Chapter 5 | Tully-Fisher Relations

ABSTRACT– In this chapter we investigate the Tully-Fisher relations using optical and near-infrared luminosities combined with kinematic information from HI rotation curves. The TF-relation has been constructed for a volume limited complete sample of spiral galaxies in the Ursa Major cluster. B, R, I and K' surface photometry and HI synthesis observations have been used. From the rotation curves, the observed maximum rotational velocity V_{max} and the amplitude of the outer flat part V_{flat} has been measured. We find that galaxies with rotation curves that are still rising at the last measured point, lie systematically on the low velocity side of the TF-relation defined by those galaxies that do show a flat part in their rotation curve. Galaxies with a partly declining rotation curve ($V_{max} > V_{flat}$) tend to lie systematically on the high velocity side of the relation when using V_{max}. However, systematic offsets are eliminated when V_{flat} is used instead of V_{max}. The tightest correlation is found for the $M_{K'}$–log2V_{flat} relation which has a slope of -10.3$\pm$0.4 and a total observed scatter of 0.29 mag, consistent with no intrinsic scatter. Although the near-infrared relation is tighter than the optical relations, as a consequence of the steeper slope in the near-infrared, K'-magnitudes do not yield a better distance tool.

1 Introduction

Numerous studies of the Tully-Fisher relations have been conducted in the past. Their aim was to find observables that reduce the scatter and thus improve this relation as a tool for measuring distances to spiral galaxies. The rapid development of optical and near-infrared detector arrays has led to greatly improved measurements of the luminosities of spiral galaxies, ranging from the originally estimated photographic B magnitudes (Tully & Fisher, 1977) to the present high quality near-infrared surface photometry (e.g. Peletier & Wilner, 1993 and Tully *et al*, 1996). Despite the apparent advantages of near-infrared luminosities (M/L is less affected by stellar population differences and extinction corrections are minimal) it has not been demonstrated convincingly so far that their use leads to a correlation with less scatter. For example, for a sample of Ursa Major spirals, Pierce & Tully (1988) found total scatters of 0.28^m and 0.31^m by using I and $H_{-0.5}$ magnitudes respectively. Bernstein *et al* (1996), using 23 spirals in Coma, also found that the H-band TF-relation has no less scatter than the I-band relation.

All the above-mentioned studies made use of the width of global HI profiles. Relatively little attention, however, has been given to the meaning of this HI line width. To some approximation, the rotational velocity of a spiral galaxy might be determined from the properly corrected width of its global HI profile. Indeed, this might be the case if the rotation curve of the HI disk rises in the inner regions and levels off to a constant velocity in the extended outer parts. However, from HI synthesis mapping of spirals it has become clear that there are two basic deviations from this classical rotation curve shape. First, many low surface brightness and dwarf galaxies only show the rising part of the rotation curve; the HI disks do not extend far enough to probe the regime of constant rotational velocity. Their *observed* maximum rotational velocity provides merely a lower limit to the actual maximum rotational velocity induced by the potential of their dark matter halo. Second, the more massive and compact galaxies often show a steep rise of the rotation curve with a maximum in the optical region followed

by a modest decline until the flat part is reached in the outer regions (e.g. Casertano & van Gorkom, 1991). Furthermore, the width and shape of the global HI profile will also be affected by the distribution of the HI gas in the disk and the possible presence of a warp or non-circular motion.

The present study is aimed at understanding the statistical properties of the relation (tightness, scatter & slope) using knowledge of the detailed shape of the HI rotation curves and of the characteristics of the galactic velocity fields. The outline of this chapter is as follows. Section 2 describes the selected galaxy sample. Section 3 gives an overview of the photometric and kinematic data available to us. Anothor 'hidden' but crucial observational ingredient for the TF-relation is the inclination angle of a galaxy which will be given some special attention. Section 4 deals with the various corrections to be applied on the observables with emphasis on the correction of the global HI profile for turbulent gas motion. Section 5 describes the TF-relations that we find in the various passbands. The fitting method will be explained and the statitical properties of the TF-relations will be examined given the shapes of the rotation curves. Section 6 discusses the necessity of an intrinsic scatter to explained the total observed scatter. In Section 7 we briefly address the issue of the Low Surface Brightness galaxies and their location on the TF-relation. In Section 8 we discuss our results in relation to other studies which consider the shape of the rotation curves. Finally, Section 9 gives a summary of our findings.

2 The sample

The spiral rich and dynamically quiescent Ursa Major cluster was selected for the present study. It has a very low velocity dispersion of $\approx$150 km/s and the 79 identified cluster members do not show any central concentration. An extensive description of this cluster is given by Tully *et al* (1996) (Chapter 1, Paper I). All 62 galaxies with an apparent magnitude brighter than m_{Zw}=14.5 are identified within a position-velocity window and they make up a complete volume limited sample. Adopting a distance to the cluster of 15.5 Mpc, this magnitude limit corresponds to an absolute magnitude of $M_B = -16.5$ and hence, the complete sample comprises all galaxies brighter than the Small Magellanic Cloud. For our current investigation, all 49 galaxies from this complete sample that are more inclined than 45° will be considered here. Positional and morphological information on these 49 galaxies are presented in Table 1.

Column (1) gives the NGC or UGC number.
Columns (2,3) provide the equatorial coordinates (1950).
Columns (4,5) provide the Galactic coordinates.
Columns (6,7) contain the Super-Galactic longitude and lattitude. The Ursa Major cluster is located in the Super-Galactic plane.
Column (8) gives the morphological type.
Column (9) provides the position angle measured anticlockwise from the north. In general this is the position angle of the receding side of the galaxy obtained from HI synthesis data. For galaxies without kinematic information this is the smallest angle between the north and the major axis.
Column (10) gives the adopted ellipticity of the stellar disk.
Column (11) contains the adopted inclination and its estimated error. See Section 3.3 for further details.
Column (12) provides the scale length in arcminutes of the exponential disk in the K'-band. At the adopted distance to the cluster of 15.5 Mpc, 1 arcmin corresponds to 4.5 kpc.
Column (13) gives the concentration index of the light. It is defined as $C_{82}=R_{80}/R_{20}$ where R_{80} and R_{20} are the radii that enclose respectively 80% and 20% of the total light. For a purely exponential disk, C_{82}=3.6.

Figure 1 shows the distribution of these 49 galaxies on the sky and in velocity. The cluster is somewhat elongated in Super-Galactic longitude, 'pointing' toward the Virgo cluster at (SGL,SGB)=(103°,-2°). A slight velocity gradient is present across the face of the cluster: galaxies with higher systemic velocities are predominantly found at lower Super-Galactic longitudes.

Of the 49 galaxies in Table 1, five S0 systems (N3990, N4026, N4111, N4143 and N4346) have either not been detected in HI by single dish telescopes and their membership relies on optical redshifts. Four more galaxies have not been observed with the WSRT (N3870 and U7129) or contain too little HI for a meaningful synthesis observation (N4117 and N4220). However, single dish profiles are available for three of these four systems; no single dish data is available for N4117 due to confusion and the WSRT observation does not go deep enough. Finally, two interacting dwarf systems (1135+48 and N3896) have their HI emission confused (in both the single dish and WSRT data) with that of their more massive companions.

This tally leaves us with a sample of 41 galaxies with measured global HI profiles. These 41 galaxies will be referred to as the '*complete sample*' in which '*complete*' relates to a lower limit on both the optical luminosity and the HI content. There are 38 galaxies in the *complete sample* with available HI synthesis data from which a more or less extended HI rotation curve has been constructed (see Chapter 3). These 38 galaxies will be referred to as the *Westerbork sample*.

We are interested in 2 aspects of the TF-relation.

Table 1: Positional and morphological information for all 49 members of the Ursa Major Cluster brighter than M_B=-16.5 and more inclined than 45°.

Name	R.A. (1950)	Dec.	l	b	SGL	SGB	Type	P.A.	$1-\frac{b}{a}$	i	$h_{K'}$	C_{82}
	h m s	° ′ ″	(°)	(°)	(°)	(°)		(°)		(°)	(′)	
(1)	(2)	(3)	(4)	(5)	(6)	(7)	(8)	(9)	(10)	(11)	(12)	(13)
U6399	11 20 35.9	51 10 09	152.08	60.96	62.02	–1.53	Sm	140	0.724	75 ± 2	0.44	3.3
U6446	11 23 52.9	54 01 21	147.56	59.14	59.72	0.22	Sd	200	0.384	51 ± 3	0.33	4.1
N3718	11 29 49.9	53 20 39	147.01	60.22	60.71	0.72	Sa	195	0.577	69 ± 3	0.94	4.6
N3726	11 30 38.7	47 18 20	155.38	64.88	66.21	–1.79	SBc	194	0.384	53 ± 2	0.63	3.1
N3729	11 31 04.9	53 24 08	146.64	60.28	60.74	0.91	SBab	164	0.318	49 ± 3	0.31	3.5
N3769	11 35 02.8	48 10 10	152.72	64.75	65.74	–0.75	SBb	150	0.691	70 ± 2	0.33	3.6
1135+48	11 35 09.2	48 09 31	152.71	64.77	65.75	–0.74	Sm	114	0.691	73 ± 3	0.23	3.6
U6667	11 39 45.3	51 52 32	146.27	62.29	62.67	1.47	Scd	88	0.878	89 ± 1	0.54	3.3
N3870	11 43 17.5	50 28 40	147.02	63.75	64.17	1.42	S0a	17	0.305	48 ± 3	0.12	7.3
N3877	11 43 29.3	47 46 21	150.72	65.96	66.68	0.38	Sc	36	0.775	76 ± 1	0.52	3.2
U6773	11 45 22.1	50 05 12	146.89	64.27	64.67	1.57	Sm	341	0.470	58 ± 3	0.28	3.3
N3893	11 46 00.2	48 59 20	148.15	65.23	65.73	1.24	Sc	352	0.331	49 ± 2	0.45	4.7
N3896	11 46 18.6	48 57 10	148.10	65.29	65.78	1.27	Sm	308	0.331	48 ± 3	0.19	6.4
N3917	11 48 07.7	52 06 09	143.65	62.79	62.97	2.74	Scd	257	0.758	79 ± 2	0.57	3.0
U6818	11 48 10.1	46 05 09	151.76	67.78	68.54	0.47	Sd	77	0.724	75 ± 3	0.33	3.4
N3949	11 51 05.5	48 08 14	147.63	66.40	66.83	1.70	Sbc	297	0.384	55 ± 2	0.32	3.7
N3953	11 51 12.4	52 36 18	142.21	62.59	62.68	3.36	SBbc	13	0.500	62 ± 1	0.71	4.4
U6894	11 52 47.3	54 56 08	139.52	60.63	60.59	4.43	Scd	269	0.844	83 ± 3	0.28	3.1
N3972	11 53 09.0	55 35 56	138.85	60.06	59.98	4.72	Sbc	298	0.724	77 ± 1	0.36	3.0
U6917	11 53 53.1	50 42 27	143.46	64.45	64.61	3.06	SBd	123	0.455	56 ± 2	0.54	3.4
N3985	11 54 06.4	48 36 48	145.94	66.27	66.56	2.34	Sm	70	0.371	51 ± 3	0.21	2.9
U6923	11 54 14.4	53 26 19	140.51	62.06	62.07	4.09	Sdm	354	0.577	65 ± 2	0.24	5.0
N3992	11 55 00.9	53 39 11	140.09	61.92	61.91	4.27	SBbc	248	0.441	56 ± 2	0.77	4.0
N3990	11 55 00.3	55 44 13	138.25	60.04	59.95	5.01	S0	40	0.500	63 ± 3	0.15	8.5
N4013	11 55 56.8	44 13 31	151.86	70.09	70.77	1.06	Sb	245	0.758	90 ± 1	0.38	3.7
N4010	11 56 02.0	47 32 16	146.68	67.36	67.69	2.26	SBd	65	0.878	89 ± 1	0.64	2.9
U6969	11 56 12.9	53 42 11	139.70	61.96	61.92	4.46	Sm	330	0.691	76 ± 2	0.25	3.0
U6973	11 56 17.8	43 00 03	153.97	71.10	71.94	0.68	Sab	40	0.609	71 ± 3	0.18	5.3
U6983	11 56 34.9	52 59 08	140.27	62.62	62.61	4.26	SBcd	270	0.344	49 ± 1	0.49	3.8
N4026	11 56 50.7	51 14 24	141.94	64.20	64.27	3.68	S0	177	0.741	84 ± 2	0.43	7.3
N4051	12 00 36.4	44 48 36	148.88	70.08	70.51	2.04	SBbc	311	0.344	49 ± 3	0.50	4.0
N4085	12 02 50.4	50 37 54	140.59	65.17	65.16	4.37	Sc	255	0.758	82 ± 2	0.29	3.2
N4088	12 03 02.0	50 49 03	140.33	65.01	65.00	4.46	Sbc	231	0.625	69 ± 2	0.62	3.0
U7089	12 03 25.4	43 25 18	149.90	71.52	71.99	2.05	Sdm	215	0.809	80 ± 3	0.57	3.5
N4100	12 03 36.4	49 51 41	141.11	65.92	65.93	4.23	Sbc	344	0.708	73 ± 2	0.47	2.9
U7094	12 03 38.5	43 14 05	150.14	71.70	72.19	2.02	Sdm	39	0.642	70 ± 3	0.27	4.5
N4102	12 03 51.3	52 59 22	138.08	63.07	62.99	5.29	SBab	38	0.441	56 ± 2	0.33	7.6
N4111	12 04 31.0	43 20 40	149.53	71.69	72.13	2.20	S0	150	0.775	90 ± 1	0.40	7.8
N4117	12 05 14.2	43 24 17	149.07	71.72	72.13	2.35	S0	21	0.562	68 ± 3	0.20	6.1
U7129	12 06 23.6	42 01 08	151.00	72.99	73.47	2.11	Sa	72	0.305	48 ± 3	...	4.4
N4138	12 06 58.6	43 57 49	147.29	71.40	71.70	2.83	Sa	151	0.371	53 ± 3	0.26	5.3
N4143	12 07 04.6	42 48 44	149.18	72.40	72.79	2.47	S0	143	0.455	60 ± 3	0.23	8.0
N4157	12 08 34.2	50 45 47	138.47	65.41	65.33	5.27	Sb	63	0.826	82 ± 3	0.48	3.9
N4183	12 10 46.5	43 58 33	145.39	71.73	71.90	3.48	Scd	346	0.861	82 ± 2	0.59	3.2
N4218	12 13 17.4	48 24 36	138.88	67.88	67.81	5.27	Sm	316	0.398	53 ± 3	0.12	3.2
N4217	12 13 21.6	47 22 11	139.90	68.85	68.82	4.96	Sb	230	0.741	86 ± 2	0.54	3.3
N4220	12 13 42.8	48 09 41	138.94	68.13	68.07	5.26	Sa	140	0.691	78 ± 3	0.29	4.2
N4346	12 21 01.2	47 16 15	136.57	69.39	69.30	6.17	S0	98	0.674	77 ± 3	0.33	8.2
N4389	12 23 08.8	45 57 41	136.73	70.74	70.65	6.16	SBbc	276	0.344	50 ± 4	0.27	3.6

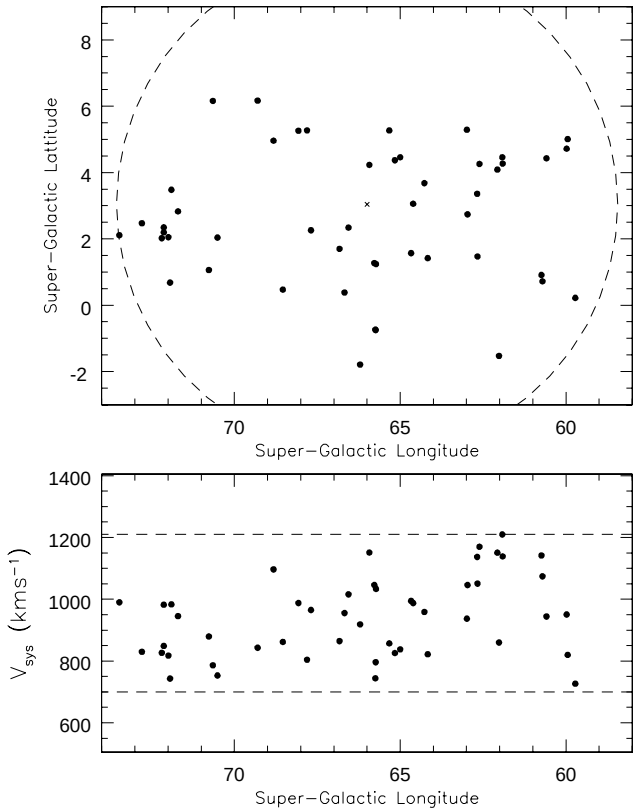

Figure 1: Distribution on the sky and in redshift of all galaxies in the cluster brighter than M_B=-16.5 and more inclined than 45°. The dashed lines indicate the boundaries of the spatial and velocity window in which the galaxies were selected.

1) The TF-relation can be considered as a manifestation of the underlying coupling between the luminosity of a galaxy and its gravitational potential. To gain some understanding of this coupling it is mandatory to map this gravitational potential. The shape of the HI rotation curve will be used to derive the shape of the potential in the plane of the galaxy. It can be expected that most will be learned from the most extreme cases. Therefore, it is important to consider a sample of galaxies with a wide range of intrinsic properties.

2) We are also interested in the accuracy of the TF-relation as an empirical tool for measuring distances to spiral galaxies. For that purpose it is important to understand the sources of scatter and identify possible objective criteria that minimize the scatter. Consequently, one often discards galaxies with extreme intrinsic properties like a very low HI content or a low surface brightness.

Both aspects justify different selection criteria when constructing the TF-relation. Therefore, we will construct 2 subsamples from the *Westerbork sample*, each optimized to address one of the two aspects mentioned above.

a) the 'unperturbed' sample

To investigate the first aspect, it is important to have a good understanding of the planar shape of the potential as inferred from the rotation curves. When deriving the rotation curve, it is assumed that the HI gas rotates around the center on circular orbits. The HI synthesis data allow us to evaluate the kinematic 'normalcy' of a gas disk from its observed velocity field. It is obvious that the assumption of circular orbits is violated in several galaxies in the *Westerbork sample*. There are 4 galaxies with close companions that show clear signs of interaction through the presence of tidal tails and extremely warped gas disks (N3718, N3769, N3893, U6973). Furthermore, there are 2 galaxies which show signs of global non-circular motion in their velocity fields (N4051, N4088). These galaxies also have a disturbed optical morphology (see Chapter 1). We have serious doubts that the derived rotation curves in these systems are reliable indicators of the potential. Excluding these 6 obviously perturbed galaxies from the *Westerbork sample* leaves us with a sample of 32 galaxies that are kinematically well behaved. We will refer to these 32 systems as the *unperturbed sample*.

b) the 'normal spiral' sample

When evaluating the TF-relation as an epirical tool to measure galaxy distances, we follow the same selection criteria as outlined by Bernstein *et al* (1994). In their study of spirals around the Coma cluster they only selected non-interacting galaxies of type Sb-Sd, with steep HI profile edges, with smooth outer isophotes and without a prominent bar. These criteria are somewhat subjective but based on global morphological characteristics that do not require detailed kinematic information on individual systems. Table 2 summarizes which galaxies from the *Westerbork sample* are excluded by these criteria. There are 15 galaxies that survive the various criteria and those 15 will be referred to as the *'normal spiral' sample*.

The Ursa Major cluster extends over roughly 15 degrees on the sky. Consequently, the depth of the sample may be considerable. The depth of the cluster is estimated by assuming that the distribution of all 79 galaxies along the line of sight is similar to the distribution along Super-Galactic longitude. From this assumption it follows that the estimated depth of the cluster contributes roughly 0.17 mag to the scatter in the TF-relation. Nevertheless, since all galaxies are nearly at the same distance, there is still little doubt about their relative luminosities, sizes and masses.

Table 2: Galaxies excluded from the *Westerbork sample* based on the selection criteria by Bernstein *et al*. Several galaxies are excluded for more than one reason.

Criteria	Excludes
non-interacting	N3769, N3893, U6973, U6818
Sb-Sd morphology	N3718, N3729, N3870, U6973, N4102, U7129, N4138, N4220 (earlier types)
	U6399, U6773, N3985, U6923, U6969, U7089, U7094, N4218 (later types)
no prominent bar	N3726, N3729, N3769, N3953, N3992, N4010, N4051, N4102, N4389
smooth outer isophotes	N3718, N3893, U6973, U6818, N3985, N4051, N4088
steep HI profile edges	N3769, N3985, N4218

3 Observables

This section describes the available data which will allow us to construct TF-relations in 4 passbands using various kinematic measures like the corrected widths of the global HI profiles and the amplitudes of the flat part of the rotation curves. Information about the various shapes of the rotation curves is also available.

3.1 Photometry

All 79 galaxies were photometrically imaged in the *B*, R_{KC} and I_{KC} passbands and 70 galaxies were imaged at K'. The University of Hawaii's 24″ and 88″ telescopes on Mauna Kea were used on 13 different runs between 1984 and 1996. Total magnitudes were obtained by integrating the exponentially extrapolated luminosity profiles. Inclination angles were derived from the optical axis ratios. A full photometric review of this sample can be found in Capter 1. One galaxy (UGC 7129) from the *complete sample* was not imaged at K'. Photometric data at various passbands are presented in Table 3.

Column (1) gives the NGC or UGC numbers.
Columns (2)-(5) contain the total apparent magnitude at the *B*, R_{KC}, I_{KC} and K' passbands. Images and luminosity profiles are presented in Chapter 1.
Column (6) provides the (extrapolated) uncorrected central surface brightness at K' of the exponential disk.
Columns (7)-(10) give the flux densities in the 60μm and 100μm bands from the IRAS Faint Source Catalog. Uncertainties are given in percentages. A total of 27 galaxies was detected while 11 galaxies are located in the IRAS incompletion gap. Two dwarf galaxies (1135+48 and N3896) are confused with their massive companions.
Columns (11) and (12) contain the 21cm radio continuum flux density or 3-sigma upper limits for extended emission in cases of non-detection.
Columns (13) and (14) provide the integrated 21cm HI flux as derived from the WSRT global profiles. The HI emissions of 1135+48 and N3896 are confused with that of their more massive neighbors, even in the WSRT datacubes. Consequently, the integrated HI fluxes of N3769 and N3893 may be slightly affected as well.
Column (15) gives the Galactic foreground extinction in the *B*-band taken from Burstein and Heiles (1984).

Uncertainties in the total magnitudes are estimated at 0.05 magnitudes in the *B*, *R* and *I* passbands and 0.08 magnitudes in the K' passband. These estimates are based on comparisons of the derived luminosities of galaxies which were observed during different runs.

3.2 Kinematics

The radio synthesis data provide HI rotation curves which, for our purposes, can be classified in three catagories as illustrated in Figure 2.

First, there are rotation curves that keep on rising continuously until the last measured point (left panel). In these cases, the *observed* maximum rotational velocity is determined by the extent of the HI disk and provides a lower limit to the actual maximum rotational velocity induced by the potential. This type of rotation curve is often observed in dwarf galaxies and in spirals with an HI disk that is confined to the inner regions. The global profiles of these galaxies are in general Gaussian or boxy and lack a clear double peaked signature.

Second, there are the 'classical' rotation curves which show a modest rise in the inner regions and then gently bend over to reach an extended flat part in the outer regions of the galaxy (middle panel). This behaviour is typical for Sb-Sd type spirals with nice exponential stellar disks. In the standard rotation curve decomposition, the amplitude of the flat part corresponds to the maximum rotational velocity of the dark halo (e.g. van Albada & Sancisi, 1986). The global profiles of these galaxies show a clear double peaked profile and the amplitude of the flat part can in general be well retrieved from the width of the global HI pro-

Table 3: Photometric information for all 49 members of the Ursa Major Cluster brighter than M_B=-16.5 and more inclined than 45°.

Name	$m_{T(B)}$	$m_{T(R)}$	$m_{T(I)}$	$m_{T(K')}$	$\mu_{0(K')}$	F_{60}	±	F_{100}	±	F_{21cm}	±	$\int$Idv	±	A_B
	– – – – – – mag – – – – – –				mag/$''^2$	Jy	%	Jy	%	– mJy –		– Jykm/s–		mag
(1)	(2)	(3)	(4)	(5)	(6)	(7)	(8)	(9)	(10)	(11)	(12)	(13)	(14)	(15)
U6399	14.33	13.31	12.88	11.09	18.72	...	..	...	..	<2.5		10.5	0.3	0.00
U6446	13.52	12.81	12.58	11.50	19.31	...	..	...	..	<7.2		40.6	0.5	0.00
N3718	11.28	9.95	9.29	7.47	17.52	0.70	10	2.29	12	11.4	0.4	140.9	0.9	0.00
N3726	11.00	9.97	9.51	7.96	17.19	3.50	6	16.95	5	49.7	5.0	89.8	0.8	0.01
N3729	12.31	10.94	10.30	8.60	16.44	2.68	6	7.38	6	18.0	0.9	5.5	0.3	0.00
N3769	12.80	11.56	10.99	9.10	16.34	2.63	5	6.78	6	12.1	2.9	62.3	0.6	0.00
1135+48	14.95	14.05	13.61	11.98	18.83	– cnf –		– cnf –		<1.6		– cnf –		0.00
U6667	14.33	13.11	12.63	10.81	18.16	...	..	...	..	<2.7		11.0	0.4	0.00
N3870	13.67	12.71	12.16	10.73	17.04	1.09	6	2.52	7			5.6[1]	1.6	0.00
N3877	11.91	10.46	9.72	7.75	15.50	5.67	4	20.30	4	35.6	2.4	19.5	0.6	0.01
U6773	14.42	13.61	13.15	11.23	18.79	...	..	...	..	<2.6		5.6	0.4	0.00
N3893	11.20	10.19	9.71	7.84	16.71	12.40	9	37.80	5	137.4	2.9	69.9	0.5	0.02
N3896	13.75	12.96	12.47	11.35	18.37	– cnf –		– cnf –		<3.1		– cnf –		0.02
N3917	12.66	11.42	10.85	9.08	17.12	0.61	8	3.16	7	<7.2		24.9	0.6	0.01
U6818	14.43	13.62	13.15	11.70	18.68	...	..	...	..	2.4	1.0	13.9	0.2	0.00
N3949	11.55	10.69	10.28	8.43	16.55	10.42	6	24.94	5	134.1	3.6	44.8	0.4	0.03
N3953	11.03	9.66	9.02	7.03	16.47	3.68	5	28.49	27	50.9	2.5	39.3	0.8	0.01
U6894	15.27	14.31	14.00	12.40	18.33	...	..	...	..	<2.7		5.8	0.2	0.00
N3972	13.09	11.90	11.34	9.39	16.50	1.01	6	3.66	6	<5.8		16.6	0.4	0.00
U6917	13.15	12.16	11.74	10.30	19.17	0.26	16	1.02	18	<4.4		26.2	0.3	0.03
N3985	13.25	12.26	11.81	10.19	17.06	1.42	6	3.42	7	9.7	1.4	15.7	0.6	0.05
U6923	13.91	12.97	12.36	11.04	17.87	0.37	12	0.90	21	<2.6		10.7	0.6	0.00
N3992	10.86	9.55	8.94	7.23	16.82	1.12	6	10.35	5	30.2	7.6	74.6	1.5	0.00
N3990[0]	13.53	12.08	11.36	9.54	16.04	...	..	...	..					0.00
N4013	12.44	10.79	9.95	7.68	14.90	5.70	6	20.13	9	36.3	0.8	41.5	0.2	0.00
N4010	13.36	12.14	11.55	9.22	17.13	1.68	9	6.76	5	16.9	1.6	38.2	0.3	0.00
U6969	15.12	14.32	14.04	12.58	19.06	...	..	...	..	<3.8		6.1	0.5	0.00
U6973	12.94	11.26	10.53	8.23	14.70	– gap –		– gap –		127.5	2.1	22.9	0.2	0.00
U6983	13.10	12.27	11.91	10.52	19.41	0.29	20	1.34	15	<5.4		38.5	0.6	0.01
N4026[0]	11.71	10.25	9.57	7.65	15.66	...	..	...	..					0.04
N4051	10.98	9.88	9.37	7.86	16.72	7.14	13	23.92	5	26.5	2.6	35.6	0.8	0.00
N4085	13.09	11.87	11.28	9.20	15.82	5.49	5	14.61	5	44.1	1.3	14.6	0.9	0.01
N4088	11.23	10.00	9.37	7.46	16.19	19.88	5	54.47	5	222.3	1.9	102.9	1.1	0.01
U7089	13.73	12.77	12.36	11.11	18.73	– gap –		– gap –		<3.4		17.0	0.6	0.00
N4100	11.91	10.62	10.00	8.02	15.77	8.10	6	21.72	4	54.3	1.7	41.6	0.7	0.04
U7094	14.74	13.70	13.22	11.58	18.56	– gap –		– gap –		<2.6		2.9	0.2	0.00
N4102	12.04	10.54	9.93	7.86	16.15	46.90	4	69.74	4	276.0	1.5	8.0	0.2	0.01
N4111[0]	11.40	9.95	9.25	7.60	15.63	– gap –		– gap –						0.00
N4117	14.05	12.47	12.47	9.98	17.11	– gap –		– gap –		3.7	1.2	6.9	1.1	0.00
U7129	14.13	12.80	12.19	...	...	– gap –		– gap –				1.1[2]		0.00
N4138	12.27	10.72	10.09	8.19	15.98	– gap –		– gap –		16.7	4.6	19.2	0.7	0.00
N4143[0]	12.06	10.55	9.84	7.86	15.23	– gap –		– gap –						0.00
N4157	12.12	10.60	9.88	7.52	14.87	12.01	6	45.43	5	179.6	2.3	107.4	1.6	0.02
N4183	12.96	11.99	11.51	9.76	17.33	– gap –		– gap –		<5.8		48.9	0.7	0.00
N4218	13.69	12.83	12.41	10.83	16.51	1.09	7	2.29	10	6.3	0.8	7.8	0.2	0.00
N4217	12.15	10.62	9.84	7.61	15.70	8.88	7	35.35	7	115.6	2.2	33.8	0.7	0.00
N4220	12.34	10.79	10.03	8.36	15.27	1.57	8	5.53	9	<4.9		4.4	0.3	0.00
N4346[0]	12.14	10.69	9.96	8.21	15.91	– gap –		– gap –						0.00
N4389	12.56	11.33	10.87	9.12	16.61	– gap –		– gap –		23.3	1.2	7.6	0.2	0.00

[0]: Not detected in HI.
[1]: from single dish data by Fisher & Tully (1981).
[2]: from single dish data by Bottinelli *et al*, in preparation. Uncertainty not provided by the authors.
– cnf –: emission confused with companion.
– gap –: located in IRAS gap.

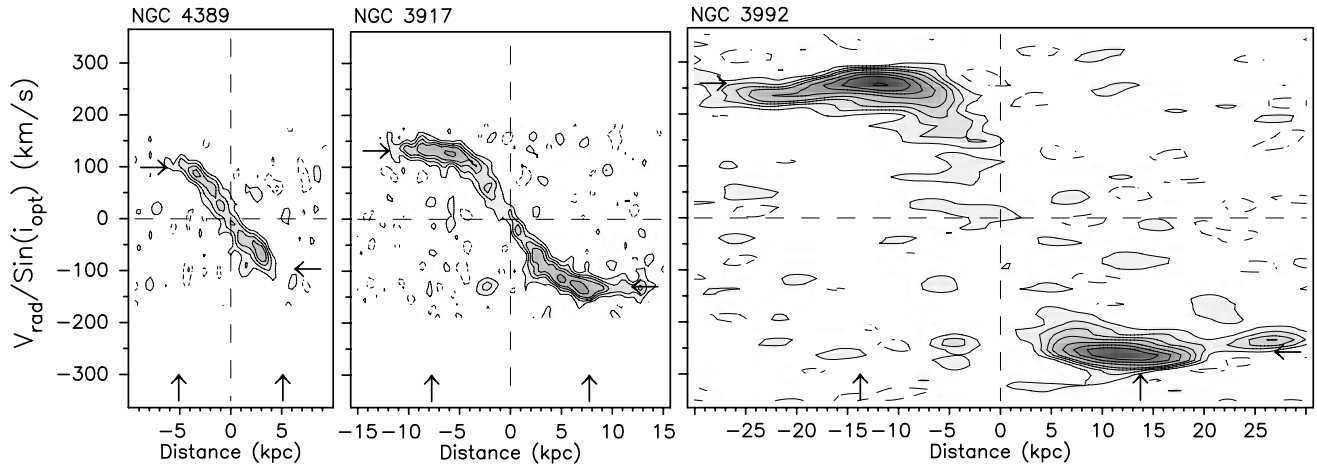

Figure 2: Proto-type examples of the three catagories of rotation curves. **Left**: Galaxy with a rotation curve that rises continuously until the last measured point. The measured maximum rotational velocity is set by the extent of the HI disk. **Middle**: The 'classical' rotation curve; a gentle rise in the central regions with a smooth transition into the extended flat part. **Right**: A rotation curve that reaches a maximum in the optical regions after which it declines somewhat to an extended flat part in the outer disk. In this case, the maximum rotation velocity exceeds the amplitude of the flat part. The vertical arrows indicate $\pm R_{25}$ and the horizontal arrows indicate the rotational velocities as inferred from the global profiles.

file. The selection criteria outlined by Bernstein *et al*, which lead to the *'normal spiral' sample*, are aimed at selecting galaxies with such a classical rotation curve like N3917, based on their global properties.

Third, there are the partly declining rotation curves which often occur in massive and compact systems (right panel). They show a steep rise in the inner regions and reach a peak rotational velocity well within the stellar disk. After this maximum they show a modest decline inside the stellar disk. In most cases this decline halts and the rotation curve extends further out with a more or less contant rotational velocity. This behaviour of the rotation curves is often seen in massive early-type spirals and in galaxies with a compact distribution of their luminous matter (e.g. Casertano & van Gorkom, 1991). In these systems, a distinction can be made between the maximum rotational velocity V_{max} and the amplitude of the flat part V_{flat}.

Off course, there are intermediate cases and cases where one side of the galaxy does show a flat part while the other side is still rising. Figure 2 also demonstrates that *the* rotational velocity of a spiral is not well-defined.

The horizontal arrows in Figure 2 indicate the rotational velocities as derived from the corrected global HI profiles. In the case of N3917, the amplitude of the flat part can be retrieved well from the global profile. In the case of N4389, the amplitude of the flat part can not be measured from the width of the global profile simply because it is not sampled by the HI disk which is confined to the inner regions of the galaxy. In the case of N3992, the width of the global profile yields the maximum rotational velocity and not the amplitude of the outer flat part. This situation arises because the bulk of the HI gas is located near the maximum rotational velocity. In general, the rotational velocities derived from the global profiles of galaxies with declining rotation curves depend on where the bulk of the HI gas is located along the rotation curve.

These examples illustrate how the line width *W is not only determined by the intrinsic maximum rotational velocity of a galaxy but also by the actual shape of the rotation curve and the distribution of the HI gas*. Even when the line width is measured very accurately, it does not guarantee a precise estimate of V_{max} or V_{flat}. Note, however, that early-type spirals are often excluded in studies of the TF-relation as a distance tool since inclusion of these galaxies increases the scatter in the relation (e.g. Rubin 1985, Pierce & Tully 1988).

In the *Westerbork sample* we have identified 10 systems with a continuously rising rotation curve (no V_{flat} available), 21 systems with a flat rotation curve (V_{max}= V_{flat}) and 7 systems with a partly declining curve ($V_{max} > V_{flat}$).

Table 4 summarizes the available kinematic data.
Column (1) gives the NGC or UGC numbers.
Columns (2)-(3) provide the uncorrected width of the global HI profiles at the 20% level of the peak flux density.
Columns (4)-(5) provide the uncorrected width of the global HI profiles at the 50% level of the peak flux density.

Column (6) gives the instrumental velocity resolution at which the HI profiles were observed.
Columns (7)-(8) contain the systemic heliocentric velocities of the galaxies.
Columns (9)-(10) contain the systemic velocities corrected for galactic rotation according to $V_{sys} = V_{hel} + 300\sin(l)\cos(b)$.
Column (11) provides information on the shape of the HI rotation curve. R: the rotation curve is still rising at the last measured point, F: the rotation curve rises monotoneously until it reaches a more or less extended flat part, D: the rotation curves shows a declining part after which it reaches an extended flat part. L denotes whether the HI distribution is lopsided, either in its extent or in its kinematics when the rotation curve rises more steeply on one side than on the other side.
Columns (12)-(13) provide the inclination corrected maximum rotational velocity derived from the rotation curve. For galaxies with a rising rotation curve (R), V_{max} is the velocity of the last measured point. For galaxies with a purely flat rotation curve (F), V_{max} is the rotational velocity averaged over the flat part. For galaxies with a declining rotation curve (D), V_{max} represents the peak velocity.
Columns (14)-(15) provide the amplitude of the flat part of the rotation curve. For galaxies with rising rotation curves (R), V_{flat} could not be measured. For galaxies with a purely flat rotation curve (F), $V_{flat} = V_{max}$. For galaxies with a declining rotation curve (D), V_{flat} is the rotational velocity averaged over the flat part.
Column (16) contains some brief comments on individual systems.

Note that the uncertainties in the line widths and recession velocities represent formal errors. The errors on V_{max} and V_{flat} included uncertainties in the inclinations (see below).

The *'normal spiral' sample* of 15 galaxies contains 8 spirals with a 'classical' rotation curve, 2 galaxies with a rising rotation curve and 5 galaxies with a partly declining rotation curve.

3.3 Inclinations

Present day instrumentation allows accurate measurements of the luminosities and global HI profiles of galaxies. In general, the observed scatter in the TF-relation is larger than can be explained by the observational uncertainties in these measured parameters alone. However, the uncertainty in corrections sensitive to inclination contribute significantly to the observed scatter. For a sample of randomly oriented galaxies more inclined than 45 degrees, an uncertainty of 1, 3 or 5 degrees in the inclination angle contributes respectively 0.04, 0.12 or 0.19 magnitudes to the scatter due to the uncertainty in line widths alone, assuming a slope in the TF-relation of −10. Therefore, it is important to determine the inclination angle of a galaxy as accurate as possible and this issue deserves some special attention.

From the photometric and HI synthesis data available to us, three independent measurements of the inclination angle of a galaxy can in principle be obtained; i_{opt} from the optical axis ratio, i_{HI} from the apparent elongation of the HI disk, and i_{VF} from fitting tilted rings to the HI velocity field. Each of these methods has its own systematic limitations which are important to recognize when estimating the actual inclination of a galaxy. In the following discussion we will briefly address those limitations and make an intercomparison of i_{opt}, i_{HI}, and i_{VF}.

a) i_{opt} from optical axis ratios

The most widely used formula to infer the inclination angle from the observed optical axis ratio (b/a)≡q was provided by Hubble (1926):

$$\cos^2(i_{opt}) = \frac{q^2 - q_0^2}{1 - q_0^2}$$

where q_0 is the intrinsic thickness of an oblate stellar disk. Holmberg (1946) determined an average value of q_0=0.20 which is still commonly used although it is obvious from images of edge-on systems that large variations in q_0 exist. For instance, Fouqué *et al* (1990) found q_0 to vary from 0.30 to 0.16 for spirals of morphological types Sa to Sd respectively and q_0=0.42 for galaxies of type Sdm-Im. Apart from the debate on the intrinsic thickness, the observed axis ratio q itself has limited meaning since it is often defined at a certain isophote around which q may still vary as a function of radius. From images of edge-on disks in the Ursa major cluster (see Chapter 1) it can often be observed that the axis ratio keeps increasing outward until the faintest isophotes. An extreme example is NGC 4389, dominated by a narrow bar and surrounded by an extended faint halo. The axis ratios presented in Table 1 were not determined at a fixed isophote but were choosen to represent the stellar disk instead of a bulge, lopsided structures or a faint halo.

b) i_{HI} from the inclined HI disk

Instead of the oblate stellar disk, the HI disk can also be used to determine the inclination. In general, the HI disk is much thinner than the stellar disk and its intrinsic thickness is of no concern. However, its patchiness, lopsidedness and the existence of warps and tidal tails may complicate the interpretation of the results from fitting ellipses to a certain HI isophote. Furthermore, the relatively large beams of synthesis arrays

Table 4: Kinematic information for the *complete sample* of 41 galaxies brighter than M_B=-16.5, more inclined than 45° and with useful global HI profiles.

Name	W_{20}	±	W_{50}	±	R	V_{hel}	±	V_{sys}	±	Shape		V_{max}	±	V_{flat}	±	Comments
	– km/s –		– km/s –		km/s	– km/s –		– km/s –				– km/s –		– km/s –		
(1)	(2)	(3)	(4)	(5)	(6)	(7)	(8)	(9)	(10)	(11)		(12)	(13)	(14)	(15)	(16)
U6399	188.1	1.4	172.5	2.9	8.3	791.5	0.6	859.7	0.6	R/F		88	5	88	5	
U6446	154.1	1.0	131.9	1.2	5.0	644.3	0.8	726.8	0.8	F	L	82	4	82	4	
N3718	492.8	1.0	465.7	1.0	33.2	993.0	0.8	1074.1	0.8	F		232	11	232	11	anomalous: extreme warp, conspicuous dustlane
N3726	286.5	1.6	260.6	1.8	5.0	865.6	0.9	918.7	0.9	F/(D)		162	9	162	9	warped
N3729	270.8	1.5	253.2	3.9	33.2	1059.8	1.4	1141.6	1.4	F		151	11	151	11	
N3769	265.3	6.7	230.5	3.6	8.3	737.3	1.8	796.0	1.8	F/(D)		122	8	122	8	interacting with 1135+48
U6667	187.5	1.4	178.1	1.9	5.0	973.2	1.2	1050.7	1.2	R	L	86	3	86	3	
N3870[1]	120	15			22	750		822		?		..	..	...	..	Markarian 186
N3877	373.4	5.0	344.5	6.2	33.2	895.4	3.8	955.2	3.8	F	L	167	11	167	11	
U6773	110.4	2.3	91.1	2.2	8.3	923.6	1.6	994.7	1.6	R	L	45	5	...	..	
N3893	310.9	1.0	277.9	4.1	5.0	967.2	1.0	1033.5	1.0	F/(D)		188	11	188	11	interacting with N3896
N3917	294.5	1.9	279.1	2.1	8.3	964.6	1.4	1045.9	1.4	F		135	3	135	3	
U6818	166.9	2.3	141.9	5.7	8.3	808.1	2.1	861.8	2.1	R/(F)	L	73	5	73	5	interacting with faint dwarf?
N3949	286.5	1.4	258.3	1.7	8.3	800.2	1.2	864.5	1.2	F	L	164	7	164	7	
N3953	441.9	2.4	413.9	3.2	33.1	1052.3	2.0	1136.9	2.0	F		223	5	223	5	
U6894	141.8	1.1	132.2	1.5	8.3	848.6	1.8	944.1	1.8	R		63	5	...	..	
N3972	281.2	1.4	260.7	5.5	8.3	852.2	1.4	950.7	1.4	R	L	134	5	...	..	
U6917	208.9	3.2	189.6	1.6	8.3	910.7	1.4	987.7	1.4	R/F		104	4	104	4	
N3985	160.2	3.7	88.0	2.4	8.3	948.2	2.0	1015.8	2.0	R		93	7	...	..	disturbed optical appearance
U6923	166.8	2.4	147.1	4.5	10.0	1061.6	2.2	1151.0	2.2	R	L	81	5	...	..	warped due to N3992?
N3992	478.5	1.4	461.4	2.4	10.0	1048.2	1.2	1138.8	1.2	F/D		272	6	242	5	
N4013	425.0	0.9	395.0	0.8	33.0	831.3	0.6	879.5	0.6	F/D		195	3	177	6	strongly warped
N4010	277.7	1.0	264.1	1.2	8.3	901.9	0.8	965.3	0.8	(R)/F	L	128	9	128	9	strongly warped
U6969	132.1	6.4	123.5	2.9	10.0	1118.5	2.4	1209.7	2.4	R		79	5	...	..	
U6973	367.8	1.8	350.4	1.2	8.3	700.5	1.0	743.1	1.0	F/D		173	10	173	10	interacting with U6962
U6983	188.4	1.3	173.0	1.1	5.0	1081.9	0.8	1170.1	0.8	F		107	7	107	7	
N4051	255.4	1.8	224.6	1.5	5.0	700.3	1.2	753.1	1.2	R/F	L	159	13	159	13	lopsided, Seyfert
N4085	277.4	6.6	255.4	7.8	19.8	745.7	5.0	825.7	5.0	R/F	L	134	6	134	6	
N4088	371.4	1.7	342.1	1.9	19.8	756.7	1.2	837.6	1.2	F/(D)	L	173	14	173	14	warped with very asymmetric velocity field
U7089	156.7	1.7	97.7	3.0	10.0	770.0	1.5	817.7	1.5	R	L	79	7	...	..	
N4100	401.8	2.0	380.5	1.8	19.9	1074.4	1.3	1151.2	1.3	F/D		195	7	164	13	
U7094	83.7	1.7	71.9	5.5	10.0	779.6	1.6	826.5	1.6	R	L	35	6	...	..	
N4102	349.8	2.0	322.4	8.5	8.3	846.3	2.0	937.1	2.0	F		178	11	178	11	LINER, HI in absorption against nucleus
U7129[2]	160	13	152	13	13	947		990		?		...	..	...	..	
N4138	331.6	4.5	266.0	7.8	19.9	893.8	3.9	945.5	3.9	F/D		195	7	147	12	
N4157	427.6	2.2	400.7	3.1	19.9	774.4	1.8	857.2	1.8	F/D		201	7	185	10	
N4183	249.6	1.2	232.5	1.5	8.3	930.1	1.0	983.5	1.0	F/D	L	115	6	109	4	
N4218	138.0	5.0	79.9	1.9	8.3	729.9	1.7	804.2	1.7	R		73	7	...	..	
N4217	428.1	5.1	395.6	3.8	33.2	1027.0	3.0	1096.7	3.0	F/D		191	6	178	5	
N4220	438.1	1.3	423.3	3.3	33.1	914.2	1.2	987.6	1.2	?		...	..	...	..	too little HI to retrieve V_{max} and V_{flat}.
N4389	184.0	1.5	164.9	1.6	8.3	718.4	1.2	786.2	1.2	R		110	8	...	..	bar dominated

[1]: from single dish data by Fisher & Tully, 1981. Value of W_{50} and uncertainty in V_{hel} not provided by the authors.

[2]: from single dish data by Bottinelli *et al*, in preparation. Errors not provided by the authors but estimated equal to the resolution.

may smooth the observed HI disks to a rounder appearance. Therefore, a simple correction for beam smearing was applied and the inclination of the HI disk was determined according to

$$\cos^2(i_{HI}) = \frac{d_{HI}^2 - \Theta_d^2}{D_{HI}^2 - \Theta_D^2}$$

where D_{HI} and d_{HI} are the observed major and minor axis diameters of the observe HI disk and Θ_D and Θ_d the sizes of the synthesized beam in the direction of the major and minor axis of the HI disk.

c) i_{VF} from HI velocity fields

The inclination angle of an HI disk can also be measured by fitting tilted-rings to its velocity field (Begeman, 1989). However, the inclination angle and the rotational velocity are strongly coupled and reasonable results can only be obtained for inclination angles between roughly 50 and 75 degree.This procedure requires accurate velocity fields with high signal-to-noise ratios as well as many independent points along a ring. The advantage that velocity fields offer is the possibility to identify warps and to check the kinematic regularity of the HI disk. For instance, the optical appearance of a galaxy may look very regular while the outer regions of the HI disk may be warped toward edge-on. Such a warp would broaden the global profile and an inclination correction based on the optical axis ratio would lead to an overestimate of the rotational velocity when dividing the line width by $\sin(i_{opt})$.

Note that the inclination measurement of a tilted ring may be affected by non-circular motions due to spiral arms, bars and lopsidedness.

d) the comparison

For the comparison between the three differently inferred inclination angles we considered only the 27 galaxies with fully reduced HI data for which the velocity fields and integrated HI maps are available (see Chapter 3). We excluded the interacting galaxies (N3769, N3893, U6973) because their outer isophotes (optical and HI) are affected by tidal tails. We also excluded galaxies with perturbed or inadequately sampled velocity fields (N4088, U6969, N4389), galaxies with excessively patchy HI maps (N4102) and obviously lopsided galaxies (N4051). These eliminations leave us with 19 galaxies that have smooth outer isophotes, well filled HI disks and regular HI velocity fields.

Figure 3 presents the comparison between the three differently inferred inclination angles using two different values for q_0. When calculating mean differences and scatters using i_{VF}, only galaxies with $i_{HI}<80°$ are

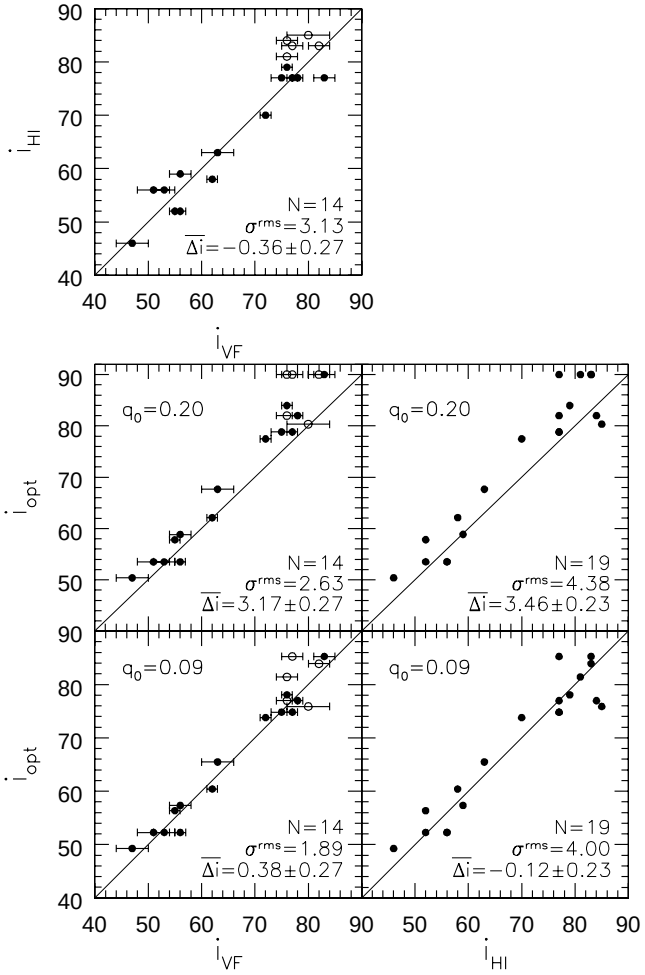

Figure 3: Intercomparison of the three independently determined inclination angles i_{opt}, i_{HI} and i_{VF}. Only the filled symbols ($i_{HI}<80°$ when i_{VF} is involved) are considered for the unweighted quantitative assessment.

considered because kinematic inclinations of highly inclined galaxies are systematically underestimated. The error bars on i_{VF} are based on the variations in i_{VF} between the various rings but are not considered any further here.

The upper most panel compares i_{VF} with i_{HI}. No significant offset is found for the 14 galaxies that meet the above-mentioned criteria. Assuming that i_{VF} and i_{HI} contribute equally to the scatter of 3.1 degrees implies that the inclination angle can be determined with an accuracy of 2.2 degrees from either the velocity fields or from the inclined HI disk. Note that the correlation turns up for $i_{HI}>80°$ due to the systematic underestimation of i_{VF} for highly inclined disks.

Comparing i_{opt} with i_{VF} and i_{HI} does show a significant offset of roughly 3 degrees when assuming q_0=0.20 (middle panels). This offset is biggest toward edge-on as would be expected in case of an overesti-

mate of the intrinsic thickness. Note that there are several galaxies with an axis ratio less than 0.20 which have been assigned an inclination angle of 90°.

This 3° offset disappears when q_0=0.09 is used (lower panels) and the rms scatter is reduced to only 1.9 degrees for i_{opt} versus i_{VF} but is still 4.0 degrees in case of i_{opt} versus i_{HI}. In the latter case, the scatter is caused by a few nearly edge-on systems for which the higher uncertainties have no influence on the deprojection of the rotational velocities.

The adopted inclinations and their errors, listed in column 11 of Table 1 are best estimates based on all the information available for a particular galaxy, including the morphology of dust lanes if present. For galaxies which lack fully reduced HI synthesis data, the inclination angles were inferred from the optical axis ratios using q_0=0.09 for galaxies of type Sc and later and q_0=0.24 for galaxies of type Sbc and earlier. The latter value of q_0 seemed justified by the observed axis ratios of the (nearly) edge-on systems N4013, N4026 and N4111 of types Sb, S0 and S0 respectively. Unfortunately, there are not enough suitable galaxies available to determine q_0 as a function of morphology.

4 Corrections

Before the observed magnitudes and linewidths can be plugged into the TF-relation, they need to be corrected for the effects of Galactic and internal extinction, projection, finite instrumental velocity resolution and the turbulent motion of the HI gas. The applied corrections will be briefly discussed below.

4.1 Corrections on the magnitude

Total apparent magnitudes $m_T(\lambda)$ as listed in Table 1 were obtained by fitting an exponential profile to the quasi linear part of the luminosity profiles and integrating these extended luminosity profiles to infinity (see Chapter 1). Because the recession velocity of our sample is only some 950 km/s, no K-corrections were applied.

a) Galactic extinction

The total magnitudes were corrected for Galactic foreground extinction using the *B*-band extinction coefficients A_B^b provided by Burstein and Heiles (1984) and the Galactic extinction law described by Rieke and Lebofsky (1985); A_R^b=0.57 A_B^b, A_I^b=0.36 A_B^b and $A_{K'}^b$=0.085 A_B^b. Values of A_B^b are listed in Table 3. The high Galactic lattitude ($60° < b < 75°$) of the cluster results in a minimal Galactic extinction with a maximum in the *B*-band of only 0.05 mag.

b) internal extinction

Total magnitudes were also corrected for internal extinction using the prescription by Tully and Fouqué (1985):

$$A_\lambda^i = -2.5\,\mathrm{Log}\,[\, f\left(1+e^{-\tau_\lambda \sec(i)}\right) + (1-2f)\left(\frac{1-e^{-\tau_\lambda \sec(i)}}{\tau_\lambda \sec(i)}\right)]$$

where f=0.1 is the fraction of stars uniformly mixed with a dust layer of opacity τ_B=0.81, τ_R=0.40, τ_I=0.28 and $\tau_{K'}$=0.035, seen under an inclination angle i as given in table 1. The values of f and τ_λ were taken from Tully *et al* (1998). For galaxies more inclined than 80°, $A_\lambda^{i=80}$ is adopted. The values of A_λ^i for inclination angles of 45° and 80° are tabulated below together with their uncertainties given an error of 3° in the inclination angle.

	inclination	
	45°±3°	80°±3°
A_B^i	0.54±0.02	1.42±0.25
A_R^i	0.29±0.01	0.94±0.20
A_I^i	0.21±0.01	0.72±0.17
$A_{K'}^i$	0.03±0.00	0.11±0.03

For highly inclined systems, the uncertainties in the internal extinctions at *B*, *R*, and *I* become quite substantial even without considering variations in (f,τ_λ) which are likely to vary from one galaxy to another. At this point, for instance, we made no distinction between dusty high surface brightness galaxies and the relatively dust-free low surface brightness galaxies.

c) absolute magnitudes

Corrected absolute total magnitudes $M_T^{b,i}(\lambda)$ were calculated assuming a common distance of 15.5 Mpc, corresponding to a distance modulus of 30.95 and thus

$$M_T^{b,i}(\lambda) = m_T(\lambda) - A_\lambda^b - A_\lambda^i - 30.95$$

4.1 Corrections on the linewidth

a) instrumental broadening

The most widely used method to correct for broadening of the global HI profiles due to a finite instrumental velocity resolution was provided by Bottinelli *et al* (1990). For the widths at the 20% and 50% levels of the peak flux they advocate

$$W_{20} = W_{20}^{obs} - 0.55\,R$$
$$W_{50} = W_{50}^{obs} - 0.13\,R$$

where R is the instrumental velocity resolution in km/s. This empirically derived prescription is based on intercomparisons of profile widths obtained at different velocity resolutions.

The corrections applied by us are based on more analytic considerations, as explained in Chapter 3. We use:

$$W_{20} = W_{20}^{\rm obs} - \delta W_{20}$$
$$W_{50} = W_{50}^{\rm obs} - \delta W_{50}$$

where

$$\delta W_{20} = 35.8 \cdot \left[\sqrt{1 + \left(\frac{R}{23.5} \right)^2} - 1 \right]$$
$$\delta W_{50} = 23.5 \cdot \left[\sqrt{1 + \left(\frac{R}{23.5} \right)^2} - 1 \right]$$

and R is the instrumental velocity resolution in km/s. The constants depend on the intrinsic steepness of the profiles for which a Gaussian shape was assumed with a dispersion of 10 km/s. The differences between Bottinelli *et al*'s and our corrections ($\Delta\delta$W = $\delta W^{Bot} - \delta W^{our}$) are only minor and tabulated below for typical instrumental resolutions of the WSRT.

level	$\Delta\delta$W				
	– – – – – R (km/s) – – – – –				
	5.0	8.3	16.5	19.9	33.1
20%	2.0	2.4	1.2	0.2	-7.8
50%	0.2	-0.3	-3.1	-4.7	-12.8

The larger differences occur for the poorest resolutions at which only the broadest profiles were observed. Consequently, the differences are a completely negligible fraction of the line widths.

b) random motions

After the correction for instrumental resolution, the profile widths were corrected for broadening due to random motions of the HI gas by applying Tully and Fouqué's (1985) formula

$$W_{R,l}^2 = W_l^2 + W_{t,l}^2 \left[1 - 2\, e^{-\left(\frac{W_l}{W_{c,l}}\right)^2} \right] - 2\, W_l\, W_{t,l} \left[1 - e^{-\left(\frac{W_l}{W_{c,l}}\right)^2} \right]$$

where the subscript l refers to the widths at the l=20% or the l=50% level of peak flux. This formula yields a linear subtraction of $W_{t,l}$ if $W_l > W_{c,l}$ and a quadratic subtraction if $W_l < W_{c,l}$. Values of $W_{t,l}$ and $W_{c,l}$ are different for line width corrections at the 20% and 50% levels. The values of $W_{c,l}$ indicate the profile widths where the transition from boxy to Gaussian occurs. The amount by which a global profile is broadened due to random motions is given by $W_{t,l}=2k_l\sigma$ where, for a Gaussian velocity dispersion σ, k_{20}=1.80 and k_{50}=1.18.

The generally adopted values for $W_{c,l}$ are $W_{c,20}$=120 km/s and $W_{c,50}$=100 km/s. The more important values of $W_{t,l}$, however, have been subject of some debate among various authors. With our new HI synthesis data we can give a meaningful contribution to this debate.

Bottinelli *et al* (1983) came up with an empirical approach, based on a minimization of the scatter in the TF-relation. They assumed an anisotropic velocity dispersion of the HI gas of σ_x=σ_y=1.5σ_z and a velocity dispersion perpendicular to the plane of σ_z=10 km/s. They determined the values of k_l by minimizing the scatter in the TF-relation and found k_{20}=1.89 and k_{50}=0.71, indicating deviations from a Gaussian distribution (broader wings). Due to the assumed velocity anisotropy, $W_{t,l}$ has become a function of inclination angle and varies in the range $45 < W_{t,20} < 57$ and $17 < W_{t,50} < 21$ for inclinations ranging between $45° < i < 90°$.

The same value of k_{20}=1.89 was adopted by Tully and Fouqué (1985) but they assumed an isotropic velocity dispersion of σ_x=σ_y=σ_z=10 km/s and consequently advocate $W_{t,20}$=2·1.89·10=38 km/s, independent of inclination. They did not address the situation at the 50% level.

Fouqué *et al* (1990) also assumed isotropy but adopted σ=12 km/s. They determined k_l in a more direct way by comparing the corrected line width to the observed maximum rotational velocity V_{max} as derived from HI velocity fields. They found k_{20}=1.96 and k_{50}=1.13, indicating a similar deviation from a Gaussian distribution as detected by Bottinelli *et al*. Consequently, Fouqué *et al* advocate the much larger values of $W_{t,20}$=47 km/s and $W_{t,50}$=27 km/s respectively.

A similar procedure was followed by Broeils (1992) using a sample of 21 galaxies with well defined HI velocity fields. Broeils made no a priori assumptions about the intrinsic velocity dispersion and did not decouple k_l and σ. He did, however, recognize that V_{max} may exceed V_{flat} and he determined for each galaxy the values of $W_{t,l}^{max}$ and $W_{t,l}^{flat}$ for which the differences

$$\Delta W_{R,l}^{\rm max} = W_{R,l} - 2{\rm V}_{\rm max}\ {\rm sin(i)}$$

and

$$\Delta W_{R,l}^{\rm flat} = W_{R,l} - 2{\rm V}_{\rm flat}\ {\rm sin(i)}$$

become zero for each galaxy. He found mean values of

$$W_{t,20}^{\rm max} = 21\pm2 \quad , \quad W_{t,50}^{\rm max} = 7\pm1$$
$$W_{t,20}^{\rm flat} = 37\pm5 \quad , \quad W_{t,50}^{\rm flat} = 25\pm4$$

(Note that he quoted scatters instead of the errors in the mean.) He rejected his results, probably discouraged by the large *scatters*, and adopted the values $W_{t,20}$=38 and $W_{t,50}$=14 km/s which he erroneously identifies with Bottinelli *et al*'s results.

Finally, Rhee (1996) performed the same investigation using 28 galaxies, most of them in common with Broeils' (1992) sample. Not surprisingly, he found

$$W_{t,20}^{\rm max} = 20\pm2 \quad , \quad W_{t,50}^{\rm max} = 8\pm2$$
$$W_{t,20}^{\rm flat} = 30\pm3 \quad , \quad W_{t,50}^{\rm flat} = 18\pm3$$

similar to Broeils' result.

Here, with our new and independent dataset, we follow the same strategy as Broeils and Rhee by investigating which values of $W_{t,l}$ allow an accurate retrieval of V_{max} and V_{flat} from the broadened global profile. For this purpose we will only consider those 22 galaxies in our Ursa Major sample that show a flat part in their rotation curves (with a significant amount of HI gas) and that are free from a major warp in inclination angle. Of these 22, there are 6 galaxies with $V_{max} > V_{flat}$. Note that both Broeils and Rhee used Bottinelli *et al*'s prescription to correct for instrumental broadening which we are forced to adopt here to ensure a valid comparison between their and our results. We calculated the values of $W_{t,l}^{\rm max}$ and $W_{t,l}^{\rm flat}$ for which the average values

$$\overline{\Delta W_{R,l}^{\rm max}} = \frac{1}{N}\sum \left({\rm W_{R,}}_l - 2{\rm V_{max}sin(i)}\right)$$
$$\overline{\Delta W_{R,l}^{\rm flat}} = \frac{1}{N}\sum \left({\rm W_{R,}}_l - 2{\rm V_{flat}sin(i)}\right)$$

become zero. This is done for both the entire sample of N=22 galaxies and for the subsample of N=16 galaxies with $V_{max} = V_{flat}$. For the entire sample we find

$$W_{t,20}^{\rm max} = 22 \quad , \quad W_{t,50}^{\rm max} = 5$$
$$W_{t,20}^{\rm flat} = 32 \quad , \quad W_{t,50}^{\rm flat} = 15$$

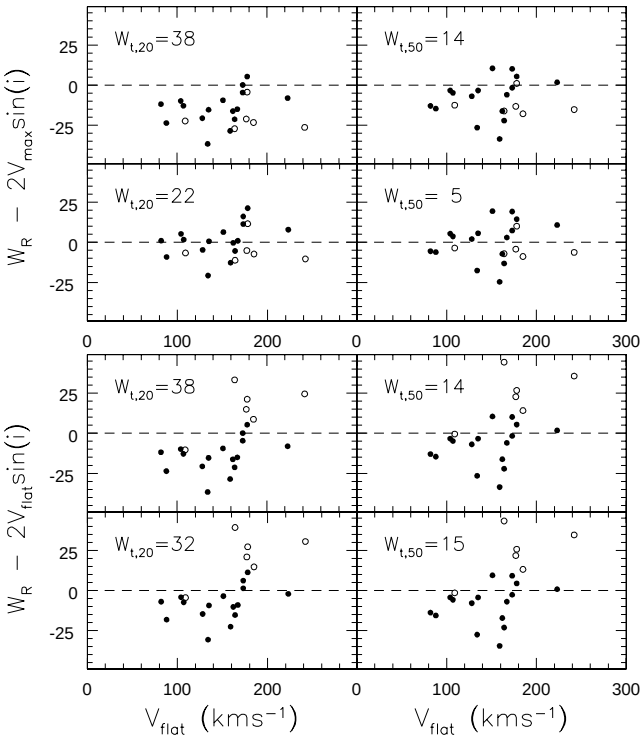

Figure 4: Comparison of the global profile widths $W_{R,l}$, corrected for instrumental broadening and random motions, with $2V_{max}$ sin(i) (Upper panels) and with $2V_{flat}$ sin(i) (lower panels). The left panels consider $W_{R,20}$ and the right panels $W_{R,50}$. Different values of the random motion parameters $W_{t,l}$ are used. Open symbol indacate galaxies with declining rotation curves ($V_{max} > V_{flat}$) and filled symbols indicated galaxies without a declining part ($V_{max} = V_{flat}$). See section 4.1 for further details.

These values are in good agreement with the (rejected) results of Broeils and in excellent agreement with the results of Rhee. The values of $W_{t,l}^{\rm flat}$ are larger than the values of $W_{t,l}^{\rm max}$ because the galaxies with $V_{max} > V_{flat}$ in our sample have considerable amounts of HI gas at their peak velocity in the rotation curve. This gas, rotating at V_{max}, broadens the global profile somewhat further. If we consider only the 16 galaxies for which $V_{max} = V_{flat}$ we find

$$W_{t,20}^{\rm max} = W_{t,20}^{\rm flat} = 23 \quad , \quad W_{t,50}^{\rm max} = W_{t,20}^{\rm flat} = 6$$

in agreement with the values of $W_{t,l}^{\rm max}$ we found when using all 22 galaxies.

Our results are illustrated in figure 4 where we show, for each of the 22 galaxies, the deviations $\Delta W_{R,l}^{\rm max}$ (upper panels) and $\Delta W_{R,l}^{\rm flat}$ (lower panels) as a function of V_{flat}. Galaxies with $V_{max} = V_{flat}$ are indicated by filled symbols, galaxies with $V_{max} > V_{flat}$ are indicated by open symbols. The upper

two panels in each block show the results one obtains when using Broeil's adopted values of $W_{t,20}$ = 38 and $W_{t,50}$ = 14 km/s.

From the upper panels in the upper block it is clear that the maximum roational velocity as derived from the corrected global profiles is severely underestimated when using the values of $W_{t,l}$ as adopted by Broeils. This systematic underestimation disappears when $W_{t,20}$ is decreased from 38 to 22 km/s and $W_{t,50}$ is decreased from 14 to 5 km/s. The upper two panels in the lower block show that if one is interested in the amplitude of the flat part, which is smaller than the maximum rotational velocity for galaxies with a declining rotation curve (open symbols), the offset becomes less significant simply because the open symbols scatter upward. In this case, to obtain an average zero offset, we find similar values for $W_{t,l}$ as those adopted by Broeils. However, we find the curious situation that the corrected width of the global profile systematically overestimates V_{flat} for galaxies with a declining rotation curve (open symbols) and systematically underestimates V_{flat} for galaxies with a purely flat rotation curve (filled symbols).

From this we can conclude that, in a statistical sense, the maximum rotational velocity of a galaxy can be reasonable well retrieved from the width of the global profile when using $W_{t,20}$ = 22 or $W_{t,50}$ = 5 km/s. The amplitude of the flat part can not be retrieved consistently for a mixed sample containing galaxies with declining rotation curves. Note that we have explored only a restricted range of rotational velocities: 80–200 km/s.

Our results also indicate a non-Gaussian distribution of random velocities in the sence that $W_{t,20}/W_{t,50} \neq 1.80/1.18$. Interpreting $W_{t,20}$ and $W_{t,50}$ in terms of velocity dispersions it follows that

$$\sigma_{20} = W_{t,20}/2k_{20} = 6.1 \text{ km/s}$$
$$\sigma_{50} = W_{t,50}/2k_{50} = 2.1 \text{ km/s}$$

where k_{20}=1.80 and k_{50}=1.18 for a Gaussian distribution. Recall, however, that we advocate a different correction for instrumental broadening than Bottinelli *et al*'s scheme used by Broeils and Rhee. With our correction method for instrumental broadening we find the somewhat smaller values of:

$$W_{t,20} = 22 \quad , \quad W_{t,50} = 2$$

These smaller values of $W_{t,l}$ allow to retrieve V_{flat} from the global profiles of galaxies with purely flat rotation curves and V_{max} for galaxies with declining rotation curves. Applying our correction method for instrumental resolution and the above-mentioned value of $W_{t,20}$ = 22 km/s we find for the 38 galaxies in the *Westerbork sample* an rms scatter in $\Delta W_{20} = 0.5W_R^i - V_{max}$ of 6.8 km/s.

Applying all the corrections discussed in this section leads to the inclinations, absolute magnitudes and values of log(W) as listed in Table 5.
Column (1) gives the NGC or UGC numbers.
Column (2) contains the adopted inclinations. These inclinations are determined with various methods.
Columns (3-6) provide the corrected absolute magnitudes. Average errors are estimated at 0.05 mag in the *B*, *R* and *I* bands and 0.08 mag at *K′*, excluding distance uncertainties.
Columns (7-9) give the three different kinematic measures.
Column (10) indicates whether a galaxy has a high (H) or a low (L) central surface brightness of the disk.
Column (11-13) identify which galaxies are a member of the *unperturbed sample* (u) and the *normal spiral sample* (ns). The last column identifies those unperturbed galaxies with a 'classical' (V_{max} = V_{flat}) rotation curve.

5 TF-relations

In this section we will discuss the TF-relations in the various bandpasses using the different kinematic measures W_R^i, V_{max} and V_{flat}.

First we will describe the applied methods of fitting and calculating the total observed scatter. Then we will make a comparison between the existing single dish data and the new WSRT data and illustrate how the statistical properties of the relations differ between the *unperturbed sample* and the *normal spiral sample* for the various passbands. Next, we will discuss how these differences in scatter and slope can be understood from a kinematic point of view using information on the shapes of the rotation curves.

5.1 Fitting method

Weighted least-squares fits were made taking error bars in both directions into account. In order to calculate a meaningful reduced chi-squared (χ^2_{Red}), the following uncertainties are considered
1) the uncertainties in $M_T^{b,i}$ due to photometric errors δm_T and uncertainties in the inclination angles δi.
2) the errors on log(W) where W is either W_R^i from the global profile or $2V_{max}$ or $2V_{flat}$ from the rotation curves. Values of δW_R^i, δV_{max} and δV_{flat} take uncertainties in the inclination δi into account.
3) additional uncertainties in absolute magnitude due to the depth of the cluster which is estimated to contribute σ_{depth}=0.17 mag in quadrature to the total observed scatter.

Table 5: Adopted inclinations, corrected absolute magnitudes and line widths for all 38 galaxies in the *Westerbork Sample*. These values were used when constructing the TF-relations. The last columns indicate to which samples a galaxy belongs.

Name	incl.	$M_T^{b,i}(B)$	$M_T^{b,i}(R)$	$M_T^{b,i}(I)$	$M_T^{b,i}(K')$	$Log(W_R^i)$	$Log(2V_{max})$	$Log(2V_{flat})$	SB	Sample		
	(°)	——— magnitude ———								u	ns	c
(1)	(2)	(3)	(4)	(5)	(6)	(7)	(8)	(9)	(10)	(11)	(12)	(13)
U6399	75 ± 2	-17.76	-18.33	-18.58	-19.93	2.235 ± 0.005	2.246 ± 0.025	2.246 ± 0.025	L	x		x
U6446	51 ± 3	-18.03	-18.46	-18.60	-19.48	2.242 ± 0.019	2.215 ± 0.021	2.215 ± 0.021	L	x	x	x
N3718	69 ± 3	-20.59	-21.53	-22.05	-23.53	2.678 ± 0.009	2.667 ± 0.021	2.667 ± 0.021	H			
N3726	53 ± 2	-20.58	-21.32	-21.68	-23.02	2.519 ± 0.012	2.511 ± 0.024	2.511 ± 0.024	H	x		x
N3729	49 ± 3	-19.22	-20.32	-20.87	-22.38	2.470 ± 0.020	2.480 ± 0.032	2.480 ± 0.032	H	x		x
N3769	70 ± 2	-19.10	-19.94	-20.36	-21.90	2.410 ± 0.013	2.387 ± 0.028	2.387 ± 0.028	H			
U6667	89 ± 1	-18.04	-18.78	-19.04	-20.25	2.222 ± 0.003	2.236 ± 0.015	2.236 ± 0.015	L	x	x	x
N3877	76 ± 1	-20.24	-21.23	-21.78	-23.28	2.525 ± 0.007	2.524 ± 0.029	2.524 ± 0.029	H	x	x	x
U6773	58 ± 3	-17.22	-17.71	-18.07	-19.76	2.052 ± 0.017	1.954 ± 0.048	... ± ...	L	x		
N3893	49 ± 2	-20.35	-21.08	-21.47	-23.14	2.582 ± 0.013	2.575 ± 0.025	2.575 ± 0.025	H			
N3917	79 ± 2	-19.65	-20.41	-20.77	-21.97	2.440 ± 0.004	2.431 ± 0.010	2.431 ± 0.010	L	x	x	x
U6818	75 ± 3	-17.66	-18.02	-18.31	-19.32	2.180 ± 0.009	2.164 ± 0.030	2.164 ± 0.030	L			
N3949	55 ± 2	-20.07	-20.62	-20.93	-22.56	2.506 ± 0.011	2.516 ± 0.019	2.516 ± 0.019	H	x	x	x
N3953	62 ± 1	-20.68	-21.71	-22.23	-23.96	2.649 ± 0.005	2.649 ± 0.010	2.649 ± 0.010	H	x		x
U6894	83 ± 3	-17.10	-17.58	-17.67	-18.66	2.094 ± 0.004	2.100 ± 0.034	... ± ...	L	x	x	
N3972	77 ± 1	-19.10	-19.82	-20.19	-21.64	2.421 ± 0.003	2.428 ± 0.016	... ± ...	H	x	x	
U6917	56 ± 2	-18.49	-19.16	-19.48	-20.69	2.351 ± 0.013	2.318 ± 0.017	2.318 ± 0.017	L	x	x	x
N3985	51 ± 3	-18.35	-19.04	-19.39	-20.79	2.255 ± 0.021	2.270 ± 0.033	... ± ...	H	x		
U6923	65 ± 2	-17.86	-18.44	-18.92	-19.95	2.204 ± 0.010	2.210 ± 0.027	... ± ...	L	x		
N3992	56 ± 2	-20.75	-21.76	-22.27	-23.75	2.738 ± 0.010	2.736 ± 0.010	2.685 ± 0.009	H	x		
N4013	90 ± 1	-19.93	-21.10	-21.72	-23.38	2.576 ± 0.001	2.591 ± 0.007	2.549 ± 0.015	H	x	x	
N4010	89 ± 1	-19.01	-19.75	-20.12	-21.84	2.404 ± 0.002	2.408 ± 0.031	2.408 ± 0.031	L	x		x
U6969	76 ± 2	-17.02	-17.36	-17.45	-18.45	2.069 ± 0.022	2.199 ± 0.027	... ± ...	L	x		
U6973	71 ± 3	-19.00	-20.26	-20.84	-22.78	2.560 ± 0.008	2.539 ± 0.025	2.539 ± 0.025	H			
U6983	49 ± 1	-18.44	-18.99	-19.26	-20.46	2.346 ± 0.007	2.330 ± 0.028	2.330 ± 0.028	L	x	x	x
N4051	49 ± 3	-20.55	-21.38	-21.80	-23.12	2.489 ± 0.020	2.502 ± 0.036	2.502 ± 0.036	H			
N4085	82 ± 2	-19.29	-20.02	-20.39	-21.86	2.393 ± 0.012	2.428 ± 0.019	2.428 ± 0.019	H	x	x	x
N4088	69 ± 2	-20.65	-21.48	-21.97	-23.54	2.559 ± 0.006	2.539 ± 0.035	2.539 ± 0.035	H	x		x
U7089	80 ± 3	-18.64	-19.12	-19.31	-19.95	2.140 ± 0.006	2.199 ± 0.038	... ± ...	L	x		
N4100	73 ± 2	-20.14	-20.98	-21.43	-23.00	2.586 ± 0.005	2.591 ± 0.016	2.516 ± 0.034	H	x	x	
U7094	70 ± 3	-17.16	-17.80	-18.13	-19.42	1.880 ± 0.012	1.845 ± 0.074	... ± ...	L	x		
N4102	56 ± 2	-19.58	-20.77	-21.28	-23.12	2.594 ± 0.011	2.551 ± 0.027	2.551 ± 0.027	H	x		x
N4138	53 ± 3	-19.30	-20.56	-21.10	-22.79	2.573 ± 0.018	2.591 ± 0.016	2.468 ± 0.035	H	x		
N4157	82 ± 3	-20.27	-21.30	-21.79	-23.54	2.600 ± 0.004	2.604 ± 0.015	2.568 ± 0.023	H	x	x	
N4183	82 ± 2	-19.41	-19.90	-20.16	-21.30	2.358 ± 0.003	2.362 ± 0.023	2.338 ± 0.016	L	x	x	
N4218	53 ± 3	-17.88	-18.45	-18.78	-20.15	2.176 ± 0.024	2.164 ± 0.042	... ± ...	H	x		
N4217	86 ± 2	-20.22	-21.27	-21.83	-23.45	2.581 ± 0.006	2.582 ± 0.014	2.551 ± 0.012	H	x	x	
N4389	50 ± 4	-18.98	-19.93	-20.30	-21.86	2.325 ± 0.026	2.342 ± 0.032	... ± ...	H	x		

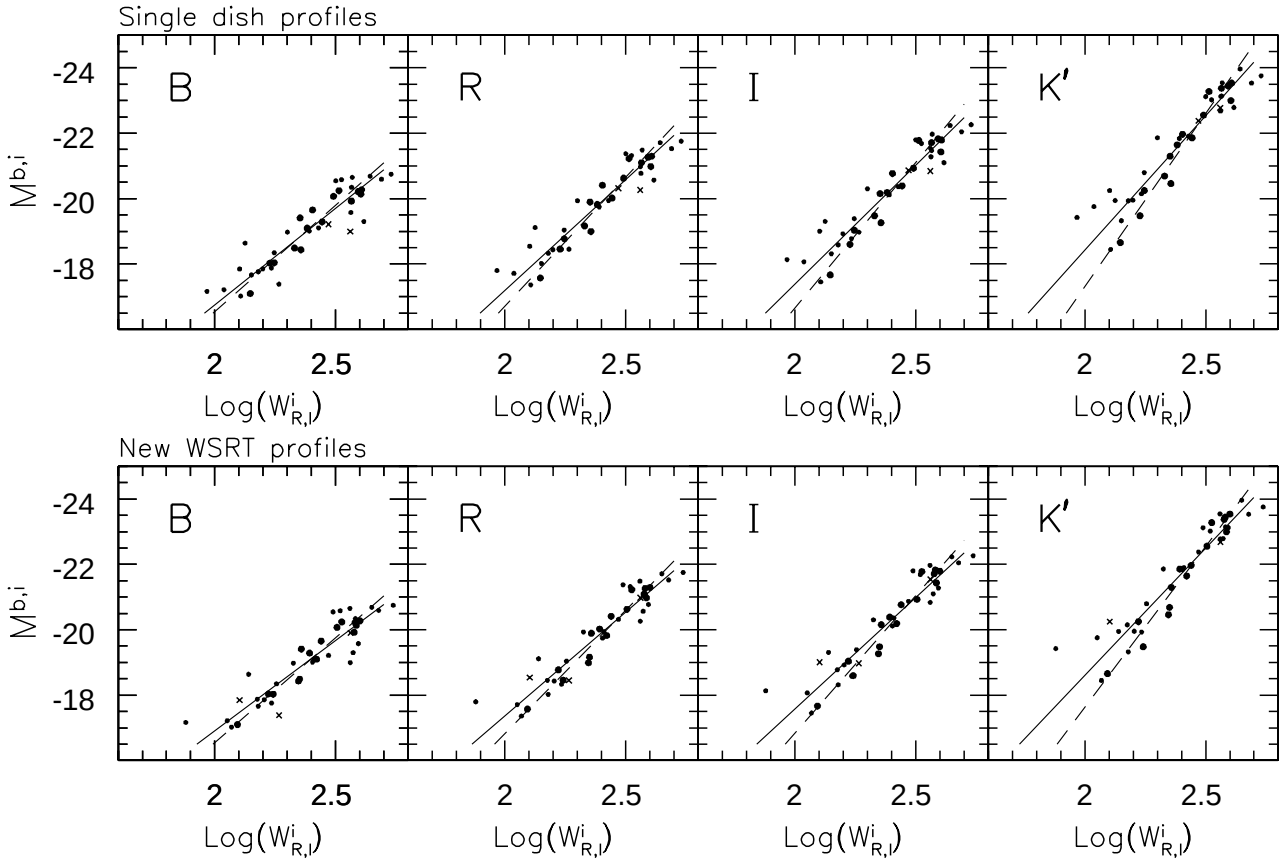

Figure 5: TF-relations using all 41 galaxies in the *complete sample* with measured global profile widths. The larger symbols indicate galaxies from the *normal spiral sample* (see Section 2). **Upper panels**: using the profile widths of single dish measurements. The two crosses represent galaxies (N3729, U6973) without single dish data due to confusion. For these galaxies the WSRT data were used. **Lower panels**: using the profile widths from the new WSRT data. The three crosses indicate galaxies (N3870, U7129, N4220) without useful synthesis data. For these galaxies the single dish data were used. For a particular bandpass, there are no significant differences between the upper and lower panels. Solid lines show the results of unweighted double regression fits to the full sample. Dashed lines indicate fits to galaxies in the *normal spiral sample*. The *normal spiral sample* defines a steeper correlation with less scatter. These differences increase systematically from B to K'.

4) the contribution from any intrinsic scatter $\sigma_{\rm intr}$, expressed in magnitudes. For the moment $\sigma_{\rm intr}$=0 mag is adopted.

The uncertainties $\delta M_T^{b,i}$ and δlog(W) were calculated by propagating the observational errors δm_T, δi and δW_{20}, $\delta V_{\rm max}$ or $\delta V_{\rm flat}$ through the correction formulas. The applied weights w_i were calculated according to

$$w_i = \frac{1}{(\delta M_T^{b,i})^2 + \sigma^2_{\rm depth} + \sigma^2_{\rm intr} + (a \cdot \delta \log(W))^2}$$

where 'a' is the fitted slope in the relation. Note that we ignored uncertainties in the Galactic extinction law, galaxy-to-galaxy variations in the parameters (f,τ_λ) used to estimate the internal extinction, the variations in the slope of the edges of the global profiles which lead to different corrections for instrumental broadening and uncertainties in the parameters (W_c,$W_{t,20}$) used to correct for random motions. Furthermore, we ignored the fact that $\delta M_T^{b,i}$ and δlog(W) are correlated through the inclination angle and its uncertainty.

One might argue against an $1/\sigma^2$ weighting because of the non-Gaussian characteristics of the errors in the corrected observables. Therefore, fits with equal weights (i.e. all points have the same error bars) were made as well by assuming for all galaxies equal relative uncertainties of 5% in W_R^i, $V_{\rm max}$ or $V_{\rm flat}$, equal photometric uncertainties of 0.05 mag in $M_T^{b,i}(B,R,I)$ and 0.08 mag in $M_T^{b,i}(K')$. These estimated average uncertainties allow to calculate a fudicial value of $\chi^2_{\rm Red}$ in order to evaluate the necessity of any intrinsic scatter

Table 6: Results from weighted least-squares fits using the widths of the global profiles. There is no significant differences when using WSRT profiles instead of single dish profiles. Note that the fit to the *normal spiral sample* yields a steeper slope and a lower scatter.

	N	Scatter				Slope		$\chi^2_{\rm Red}$		$\Gamma(\frac{N-2}{2}, \frac{\chi^2}{2})$	
		rms		bi-weight							
		S.D.	WSRT	S.D.	WSRT	S.D.	WSRT	S.D.	WSRT	S.D.	WSRT
equal weights											
Complete Sample											
B	41	0.47	0.46	0.48	0.47	-5.7 ± 0.2	-5.6 ± 0.2	4.99	4.88	0.00	0.00
R	41	0.44	0.44	0.46	0.43	-6.6 ± 0.2	-6.5 ± 0.2	3.87	3.95	0.00	0.00
I	41	0.47	0.47	0.48	0.46	-7.1 ± 0.2	-6.9 ± 0.2	4.10	4.23	0.00	0.00
K′	40	0.53	0.53	0.55	0.51	-8.1 ± 0.2	-7.8 ± 0.2	4.46	4.69	0.00	0.00
Normal Spiral Sample											
B	15	0.32	0.26	0.35	0.28	-6.8 ± 0.4	-6.5 ± 0.4	2.16	1.52	0.01	0.10
R	15	0.31	0.26	0.33	0.28	-8.0 ± 0.5	-7.7 ± 0.4	1.76	1.30	0.04	0.21
I	15	0.34	0.28	0.36	0.32	-9.0 ± 0.5	-8.6 ± 0.5	1.87	1.42	0.03	0.14
K′	15	0.34	0.32	0.39	0.34	-10.7 ± 0.6	-10.2 ± 0.5	1.54	1.42	0.10	0.14
unequal weights											
Complete Sample											
B	41	0.47	0.45	0.48	0.46	-5.9 ± 0.2	-5.5 ± 0.2	3.67	4.92	0.00	0.00
R	41	0.42	0.43	0.46	0.44	-6.8 ± 0.2	-6.4 ± 0.2	2.69	4.39	0.00	0.00
I	41	0.43	0.45	0.49	0.46	-7.3 ± 0.2	-6.8 ± 0.2	2.80	4.99	0.00	0.00
K′	40	0.47	0.51	0.55	0.51	-8.2 ± 0.3	-7.8 ± 0.2	3.03	6.22	0.00	0.00
Normal Spiral Sample											
B	15	0.33	0.27	0.34	0.28	-6.5 ± 0.5	-6.4 ± 0.4	1.85	1.87	0.03	0.03
R	15	0.32	0.27	0.33	0.27	-7.9 ± 0.6	-7.5 ± 0.4	1.61	1.93	0.07	0.02
I	15	0.36	0.29	0.36	0.31	-8.9 ± 0.6	-8.4 ± 0.4	1.82	2.40	0.04	0.00
K′	15	0.35	0.31	0.38	0.36	-10.6 ± 0.7	-9.9 ± 0.3	1.52	2.69	0.10	0.00

to explain the total observed scatter.

The total observed scatter was calculated according to

$$\sigma^2_{\rm obs} = \frac{\sum_i w_i \left[{\rm M}^{\rm b,i}_{\rm T}({\rm obs})_i - \left({\rm a}\cdot\log({\rm W}_i) + {\rm b} \right) \right]^2}{\sum_i w_i}$$

where w_i was calculated as above and 'a' and 'b' are the fitted slope and intercept.

Since the rms scatter may be strongly affected by outliers, it often does not represent the scatter of the bulk of the data points. Therefore, we find it useful to calculate the more robust bi-weight scatter $\sigma^{\rm bi}$ (see Beers *et al*, 1990) as well. Values of $\sigma^{\rm bi}$ were determined after a least-squares fit was made. For a pure Gaussian distribution of residuals one would find $\sigma^{\rm rms}$=$\sigma^{\rm bi}$. The results of both weighted and unweighted fits are given in the subsequent tables as well as $\sigma^{\rm rms}_{\rm (w)}$ and $\sigma^{\rm bi}$.

We will end this section by noting that a tighter TF-relation does not necessarily imply a better distance tool. The tightness of the relation is expressed by $\chi^2_{\rm Red}$ which is calculated by considering errors in both directions. The usefulness of the TF-relation as a distance tool, however, depends on the scatter in the vertical direction which is related to the steepness of the slope. Consequently, a tighter correlation with a steeper slope may still display a larger scatter.

5.2 Single dish versus synthesis data

Figure 5 presents a comparison between TF-relations constructed with single dish HI data (upper panels) and those constructed with the new WSRT synthesis data (lower panels) using the widths of the global profiles. There are 41 galaxies with measured global profile widths of which one galaxy (U7129) is not imaged at *K′*. There are two galaxies without single dish data because of confusion (N3729, U6973) and there are three galaxies without (useful) synthesis data (N3870,U7129,N4220). These galaxies are indicated by crosses and the sources of their profile widths are exchanged between the upper and lower panels. The larger symbols (filled circles) indicate the 15 galaxies from the *normal spiral sample*. Results of the various fits are collected in Table 6.

First we consider the *complete sample* and make a

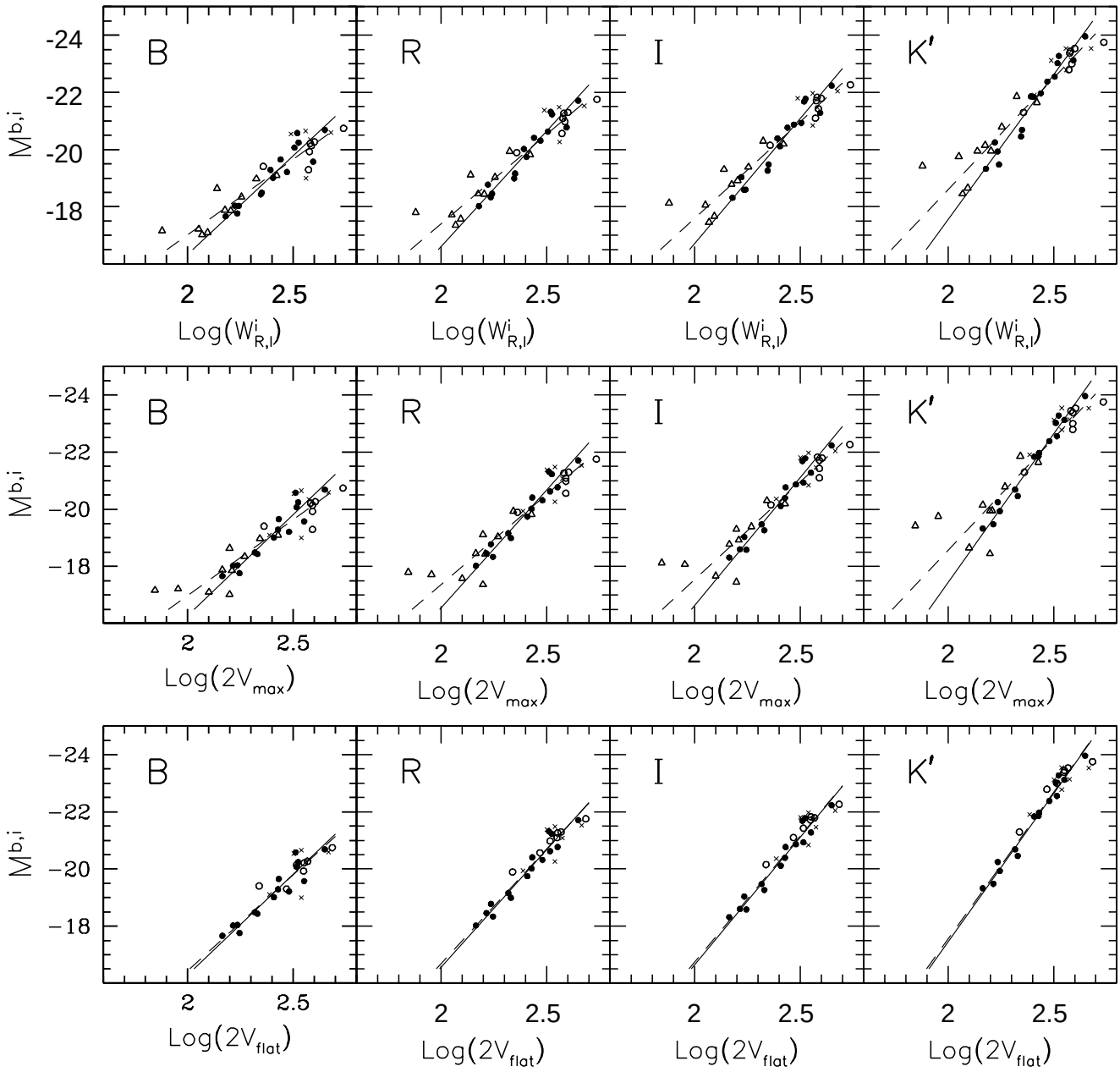

Figure 6: TF-relations for all 38 galaxies in the *Westerbork sample* with measured rotation curves. The relations are constructed for each of the 4 available passbands using 3 different kinematic measures; the corrected width of the global profile (upper row), the maximum rotational velocity measured from the rotation curve (middle row) and the amplitude of the flat part of the rotation curve (lower row). The open triangles indicate galaxies with continuously rising rotation curves (no V_{flat} measured: see left panel of Figure 2), the open circles indicate galaxies with a declining part in their rotation curves ($V_{max} > V_{flat}$: see right panel of Figure 2) and the filled symbols indicate galaxies with a flat rotation curve ($V_{max} = V_{flat}$: see middle panel of Figure 2). Crosses represent the kinematically perturbed galaxies. Solid lines show the fits to the 15 filled circles only. The dashed lines show fits using all galaxies from the *unperturbed sample* in each panel.

comparison between the TF-relations constructed with global profile widths from single dish data on the one hand and from the new WSRT data on the other hand. There are no significant differences in the scatter between the upper and lower panel of a particular passband. The slopes are insignificantly steeper when using single dish profiles. The differences are small but systematic over the 4 passbands, however, and can be accounted for by the effect of a single galaxy, U7094; the most lower-left point in the lower panels. In the single dish measurement, this galaxy is probably confused with U7089, which results in a broader single dish profile. When using unequal weights, the larger values of $\chi^2_{\rm Red}$ using the WSRT data are caused by the smaller formal errors in the global profile widths from the WSRT. Note also that using equal or unequal weights does not make a big difference to the fitted slope and scatter except for somewhat smaller values of $\chi^2_{\rm Red}$ when using single dish profiles with unequal weights. We therefore conclude that the use of an HI synthesis array does not significantly influence the statistical properties of the TF-relation for the complete sample. In Chapter 3 it was already concluded that the width and flux content of global profiles obtained with single dish telescopes and the WSRT are statistically equivalent.

Now, let's stick to the *complete sample* and consider the differences between the various passbands. First of all, it is striking to see how the slope of the relation steepens from -5.6 to -7.8 when going from the blue to the near-infrared. The scatter in the relation is similar in the optical bands but is slightly increased at K' due to the steeper slope. From the fact that $\sigma^{\rm rms} \approx \sigma^{\rm bi}$ we conclude that the residuals have a nearly Gaussian distribution.

More interesting is the fact that in each panel, the *normal spiral sample* of 15 galaxies defines a much tighter correlation with a steeper slope and significantly less scatter. At K', the slope becomes slightly steeper than -10. Furthermore, the scatter in the *normal spiral sample* becomes somewhat smaller when using the WSRT profiles instead of the single dish profiles. However, if one calculates the relative uncertainty in the scatter as $\frac{\Delta\sigma}{\sigma} = \frac{1}{\sqrt{2N}}$, the significance of this decrease in the scatter is on average only at the 0.7-sigma level. Nevertheless, it happens at all four passbands and for both $\sigma^{\rm rms}$ and $\sigma^{\rm bi}$. Note that the slope is on average 5% shallower for the WSRT data and, of course, the scatter in the vertical direction is related to the slope. The fact that $\sigma^{\rm bi}$ is slightly larger than $\sigma^{\rm rms}$ indicates that the residuals have a somewhat broader tail than would be expected from a Gaussian distribution.

In the next section we will show that the statistical differences between the *complete sample* and the *normal spiral sample* can be understood when considering the detailed kinematics of individual galaxies

5.3 TF-relations and the shapes of rotation curves

Figure 6 shows the TF-relations in all four passbands, constructed for the *Westerbork sample* of 38 galaxies which have measured rotation curves. The TF-relations in the upper panels were constructed using the corrected width of the global profiles. The relations in the middle panels were constructed using $V_{\rm max}$ from the rotation curve. The lower panels show the relations using the amplitude $V_{\rm flat}$ of the flat part of the rotation curve. The various symbols refer to the kinematical status of a galaxy:
Crosses: galaxies involved in strong interactions or with severe kinematic distortions (6 systems).
Open triangles: galaxies with rotation curves still rising at the last measured point (10 systems).
Filled circles: galaxies with monotonically rising rotation curves that bend over into a more or less extended flat part (15 systems).
Open circles: galaxies with a declining part in their rotation curve (7 systems).

The open triangles could not be included in the lower panels simply because $V_{\rm flat}$ could not be measured.

The results of the various fits are collected in Tables 7a and 7b. Table 7a contains the results obtained by applying equal weights and Table 7b gives the results obtained by applying unequal weights. Separate fits were made to the *Westerbork sample* (38 points), the *unperturbed sample* (32 points) and the *normal spiral sample* (15 points). In addition, fits were made considering only those 15 galaxies with a 'classical' rotation curve ($V_{\rm max} = V_{\rm flat}$; filled circles). To allow a meaningful comparison of the statistical properties of the correlation at a certain passband, one should consider the same sample in all three the rows. Therefore, fits in the upper and middle panels were also made considering only those galaxies that appear in the lower panels for a certain sample.

The solid lines in Figure 6 indicate least-squares fits to the filled symbols only, applying equal weights. The dashed lines show fits to the entire *normal spiral sample* (32 galaxies in the upper and middle panels and 22 galaxies in the lower panels).

From Figure 6 and Tables 7a and 7b we note the following:

- When using the corrected widths of global profiles, the TF-relation displays a larger scatter in the near-infrared than in the optical passbands, regardless of the sample This larger scatter is due to the steeper slope of the relation in the near-infrared.

- Galaxies with a 'classical' rotation curve ($V_{\rm max} = V_{\rm flat}$, filled circles in Figure 6) define a

Table 7a: Statistical properties of the Tully-Fisher relations in the various passbands, using three different kinematic measures; the corrected width of the global HI profile (W^i_R), the maximum rotational velocity ($2V_{max}$) and the amplitude of the flat part ($2V_{flat}$). The results for 3 different samples are given. There are 10 galaxies without V_{flat} in the *Westerbork sample* and the *unperturbed sample* and 2 galaxies without V_{flat} in the *normal spiral sample*. Fits with equal weights were made and errors in both directions were taken into account.

		Scatter						Slope			χ^2_{Red}			$\Gamma(\frac{N-2}{2}, \frac{\chi^2}{2})$		
		Root Mean Square			Bi-weight											
		$W^i_{R,I}$	$2V_{max}$	$2V_{flat}$	$W^i_{R,I}$	$2V_{max}$	$2V_{flat}$	$W^i_{R,I}$	$2V_{max}$	$2V_{flat}$	$W^i_{R,I}$	$2V_{max}$	$2V_{flat}$	$W^i_{R,I}$	$2V_{max}$	$2V_{flat}$
Westerbork Sample																
N=38	B	0.44	0.47		0.45	0.47		-5.4 ± 0.2	-5.5 ± 0.2		5.85	5.21		0.00	0.00	
	R	0.43	0.48		0.43	0.44		-6.3 ± 0.2	-6.4 ± 0.2		5.28	4.85		0.00	0.00	
	I	0.46	0.52		0.45	0.45		-6.8 ± 0.2	-7.0 ± 0.2		5.80	5.48		0.00	0.00	
	K′	0.53	0.63		0.50	0.50		-7.8 ± 0.2	-8.0 ± 0.2		6.36	6.68		0.00	0.00	
N=28	B	0.45	0.44	0.40	0.45	0.44	0.39	-6.0 ± 0.3	-6.3 ± 0.3	-6.8 ± 0.3	5.73	4.25	3.30	0.00	0.00	0.00
	R	0.38	0.36	0.33	0.38	0.36	0.34	-7.2 ± 0.3	-7.4 ± 0.3	-8.0 ± 0.4	3.83	2.54	2.00	0.00	0.00	0.00
	I	0.38	0.36	0.34	0.40	0.37	0.36	-7.9 ± 0.3	-8.1 ± 0.3	-8.7 ± 0.4	3.72	2.35	1.90	0.00	0.00	0.01
	K′	0.39	0.36	0.34	0.40	0.36	0.35	-9.2 ± 0.3	-9.4 ± 0.4	-10.0 ± 0.4	3.30	1.95	1.56	0.00	0.01	0.05
Unperturbed Sample																
N=32	B	0.40	0.43		0.41	0.44		-5.3 ± 0.2	-5.3 ± 0.2		4.83	4.61		0.00	0.00	
	R	0.41	0.47		0.41	0.42		-6.3 ± 0.2	-6.3 ± 0.2		5.00	4.86		0.00	0.00	
	I	0.45	0.53		0.44	0.44		-6.8 ± 0.2	-6.8 ± 0.2		5.80	5.75		0.00	0.00	
	K′	0.55	0.66		0.51	0.52		-7.8 ± 0.2	-7.8 ± 0.2		6.95	7.49		0.00	0.00	
N=22	B	0.38	0.37	0.32	0.39	0.36	0.32	-6.0 ± 0.3	-6.1 ± 0.3	-6.7 ± 0.4	4.19	3.26	2.22	0.00	0.00	0.00
	R	0.32	0.31	0.26	0.33	0.30	0.27	-7.3 ± 0.3	-7.3 ± 0.3	-8.0 ± 0.4	2.90	1.93	1.31	0.00	0.01	0.21
	I	0.33	0.31	0.28	0.35	0.31	0.29	-8.0 ± 0.3	-8.0 ± 0.4	-8.8 ± 0.4	2.98	1.84	1.32	0.00	0.02	0.20
	K′	0.37	0.33	0.29	0.37	0.29	0.29	-9.3 ± 0.3	-9.4 ± 0.4	-10.3 ± 0.4	3.00	1.63	1.17	0.00	0.06	0.33
Normal Spiral Sample																
N=15	B	0.26	0.25		0.28	0.26		-6.3 ± 0.3	-6.4 ± 0.4		2.35	1.49		0.01	0.16	
	R	0.26	0.23		0.27	0.24		-7.4 ± 0.3	-7.5 ± 0.4		2.09	1.11		0.02	0.43	
	I	0.28	0.25		0.30	0.25		-8.3 ± 0.3	-8.4 ± 0.4		2.44	1.20		0.01	0.35	
	K′	0.32	0.24		0.36	0.25		-9.8 ± 0.3	-9.9 ± 0.5		2.49	0.89		0.01	0.64	
N=13	B	0.27	0.25	0.24	0.30	0.28	0.22	-6.1 ± 0.4	-6.2 ± 0.5	-6.9 ± 0.5	2.66	1.65	1.35	0.01	0.12	0.26
	R	0.27	0.23	0.22	0.28	0.25	0.24	-7.4 ± 0.4	-7.4 ± 0.5	-8.3 ± 0.6	2.35	1.22	1.00	0.02	0.35	0.53
	I	0.30	0.26	0.25	0.32	0.27	0.26	-8.3 ± 0.4	-8.4 ± 0.5	-9.3 ± 0.6	2.77	1.35	1.11	0.00	0.26	0.43
	K′	0.34	0.26	0.24	0.35	0.26	0.26	-9.9 ± 0.4	-10.1 ± 0.6	-11.2 ± 0.7	2.90	1.01	0.76	0.00	0.52	0.75
Only galaxies with $V_{max} = V_{flat}$.																
N=15	B	0.35	0.32	0.32	0.37	0.32	0.32	-6.9 ± 0.4	-7.1 ± 0.4	-7.1 ± 0.4	3.58	2.26	2.26	0.00	0.01	0.01
	R	0.31	0.26	0.26	0.33	0.31	0.31	-8.1 ± 0.4	-8.3 ± 0.5	-8.3 ± 0.5	2.70	1.35	1.35	0.00	0.24	0.24
	I	0.32	0.27	0.27	0.36	0.29	0.29	-8.7 ± 0.4	-8.9 ± 0.5	-8.9 ± 0.5	2.82	1.30	1.30	0.00	0.27	0.27
	K′	0.33	0.22	0.22	0.34	0.24	0.24	-10.1 ± 0.4	-10.4 ± 0.6	-10.4 ± 0.6	2.39	0.72	0.72	0.01	0.80	0.80

Table 7b: Same as Table 7a but in this case unequal weights were taken into account.

		Scatter						Slope			$\chi^2_{\rm Red}$			$\Gamma(\frac{N-2}{2}, \frac{\chi^2}{2})$		
		Root Mean Square			Bi-weight											
		$W^i_{R,I}$	$2V_{max}$	$2V_{flat}$	$W^i_{R,I}$	$2V_{max}$	$2V_{flat}$	$W^i_{R,I}$	$2V_{max}$	$2V_{flat}$	$W^i_{R,I}$	$2V_{max}$	$2V_{flat}$	$W^i_{R,I}$	$2V_{max}$	$2V_{flat}$
Westerbork Sample																
N=38	B	0.44	0.44		0.45	0.48		-5.4 ± 0.2	-5.9 ± 0.2		4.95	3.51		0.00	0.00	
	R	0.43	0.40		0.43	0.42		-6.3 ± 0.2	-7.0 ± 0.2		4.69	2.77		0.00	0.00	
	I	0.45	0.43		0.45	0.43		-6.8 ± 0.2	-7.6 ± 0.2		5.41	2.95		0.00	0.00	
	K′	0.51	0.48		0.49	0.43		-7.8 ± 0.2	-8.8 ± 0.3		6.62	3.34		0.00	0.00	
N=28	B	0.44	0.42	0.37	0.45	0.43	0.38	-6.1 ± 0.3	-6.1 ± 0.3	-6.6 ± 0.3	5.31	3.64	2.57	0.00	0.00	0.00
	R	0.37	0.34	0.31	0.38	0.36	0.34	-7.2 ± 0.3	-7.1 ± 0.3	-7.6 ± 0.3	3.82	2.20	1.64	0.00	0.00	0.03
	I	0.38	0.34	0.32	0.40	0.37	0.36	-7.9 ± 0.3	-7.8 ± 0.3	-8.3 ± 0.3	3.89	2.09	1.64	0.00	0.00	0.03
	K′	0.38	0.35	0.33	0.40	0.37	0.35	-9.1 ± 0.3	-8.9 ± 0.3	-9.6 ± 0.4	3.72	2.00	1.57	0.00	0.00	0.05
Unperturbed Sample																
N=32	B	0.39	0.40		0.41	0.42		-5.3 ± 0.2	-5.7 ± 0.2		4.01	3.14		0.00	0.00	
	R	0.41	0.39		0.41	0.39		-6.2 ± 0.2	-6.9 ± 0.2		4.33	2.72		0.00	0.00	
	I	0.45	0.42		0.44	0.41		-6.7 ± 0.2	-7.6 ± 0.3		5.32	3.04		0.00	0.00	
	K′	0.53	0.49		0.51	0.42		-7.8 ± 0.2	-8.8 ± 0.3		7.24	3.63		0.00	0.00	
N=22	B	0.38	0.37	0.31	0.39	0.36	0.31	-6.0 ± 0.3	-5.9 ± 0.3	-6.6 ± 0.3	4.06	3.15	1.91	0.00	0.00	0.01
	R	0.33	0.31	0.26	0.33	0.30	0.28	-7.3 ± 0.3	-7.0 ± 0.3	-7.7 ± 0.4	2.98	1.95	1.25	0.00	0.01	0.26
	I	0.34	0.31	0.28	0.35	0.31	0.30	-8.0 ± 0.3	-7.7 ± 0.3	-8.4 ± 0.4	3.21	1.94	1.35	0.00	0.01	0.18
	K′	0.36	0.33	0.30	0.37	0.32	0.30	-9.3 ± 0.3	-9.0 ± 0.3	-9.8 ± 0.4	3.52	1.99	1.43	0.00	0.01	0.13
Normal Spiral Sample																
N=15	B	0.27	0.24		0.28	0.25		-6.4 ± 0.4	-6.2 ± 0.4		2.03	1.36		0.03	0.23	
	R	0.27	0.22		0.27	0.23		-7.5 ± 0.4	-7.3 ± 0.4		2.09	1.02		0.02	0.51	
	I	0.29	0.24		0.31	0.25		-8.4 ± 0.4	-8.2 ± 0.4		2.60	1.16		0.00	0.38	
	K′	0.31	0.22		0.36	0.24		-9.9 ± 0.3	-9.8 ± 0.5		2.92	0.91		0.00	0.62	
N=13	B	0.28	0.25	0.23	0.30	0.28	0.23	-6.3 ± 0.4	-6.0 ± 0.4	-6.8 ± 0.5	2.36	1.52	1.23	0.02	0.18	0.34
	R	0.28	0.22	0.21	0.29	0.24	0.23	-7.6 ± 0.4	-7.2 ± 0.5	-8.1 ± 0.6	2.40	1.10	0.94	0.01	0.44	0.58
	I	0.31	0.24	0.24	0.33	0.27	0.26	-8.5 ± 0.4	-8.1 ± 0.5	-9.1 ± 0.6	3.00	1.27	1.11	0.00	0.31	0.43
	K′	0.33	0.23	0.22	0.35	0.26	0.26	-10.0 ± 0.4	-9.8 ± 0.5	-10.9 ± 0.6	3.40	1.04	0.85	0.00	0.50	0.67
Only galaxies with $V_{max} = V_{flat}$.																
N=15	B	0.36	0.30	0.30	0.37	0.32	0.32	-6.8 ± 0.4	-7.0 ± 0.4	-7.0 ± 0.4	3.88	1.92	1.92	0.00	0.04	0.04
	R	0.31	0.25	0.25	0.33	0.29	0.29	-8.0 ± 0.4	-8.1 ± 0.4	-8.1 ± 0.4	3.01	1.22	1.22	0.00	0.33	0.33
	I	0.33	0.26	0.26	0.36	0.28	0.28	-8.7 ± 0.4	-8.7 ± 0.5	-8.7 ± 0.5	3.24	1.21	1.21	0.00	0.34	0.34
	K′	0.32	0.21	0.21	0.34	0.23	0.23	-10.1 ± 0.4	-10.1 ± 0.5	-10.1 ± 0.5	2.91	0.68	0.68	0.00	0.83	0.83

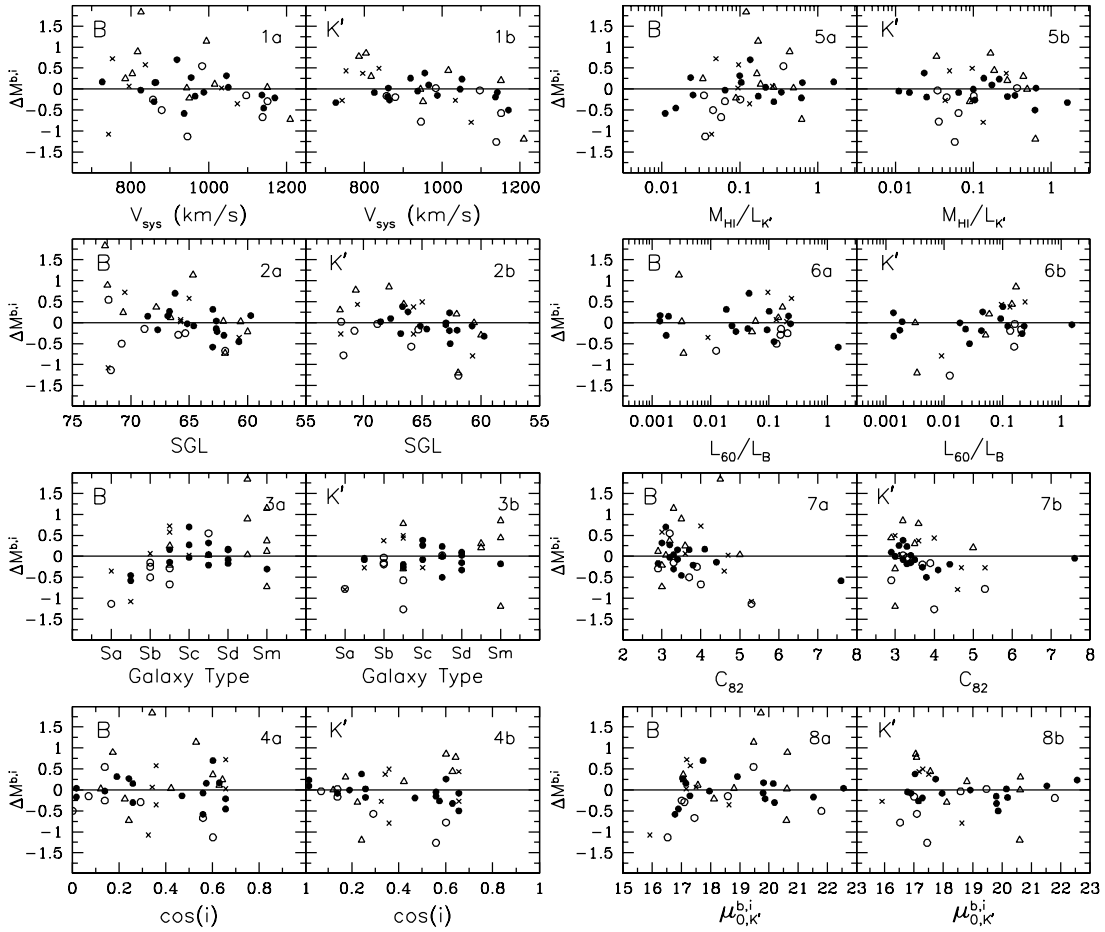

Figure 8: (**A**) Deviations of the B,K'–V_{max} TF-relations from the B,K'-V_{flat} TF-relations as a function of various global properties of spiral galaxies: 1) systemic velocity, 2) Super-Galactic Longitude, 3) morphological type, 4) inclination angle, 5) relative HI content, 6) relative dust content, 7) compactness of the radial light distribution and 8) face-on central K' surface bightness of the fitted exponential disk. Only galaxies from the *unperturbed sample* are considered and the B,K'-V_{flat} TF-relations were constructed for the 22 galaxies in this *unperturbed sample* which show a flat part in their rotation curves. Filled circles: galaxies with $V_{max} = V_{flat}$ open circles: galaxies with $V_{max} > V_{flat}$ and open triangles: galaxies without V_{flat}.

steeper and tighter relation compared to the entire sample.

- Galaxies with a rotation curve that is still rising at the last measured point (open triangles) lie systematically on the low velocity side of the relations defined by the galaxies with $V_{max} = V_{flat}$ (solid lines in Figure 6). These galaxies are mainly found among the fainter systems in the sample. If the HI disks of those galaxies would have been more extended, they most likely would have probed higher velocities further out into the halo and consequently, those galaxies would have shifted towards the relation.

- Galaxies with a partly declining rotation curve ($V_{max} > V_{flat}$; open circles) in the upper and middle panels tend to lie systematically on the high velocity side compared to galaxies with $V_{max} = V_{flat}$ of the same luminosity. If the lower amplitude V_{flat} of the flat part is used instead of the higher V_{max} values, these galaxies shift toward the relation and line up with galaxies that have a 'classical' rotation curve as is illustrated in the lower panels. Galaxies with declining rotation curves are mainly found among the brightest systems in the sample.

- When considering only the 22 galaxies in the *normal spiral sample* which show a flat part in their rotation curves, the correlation becomes tighter from the blue to the near-infrared. Furthermore, the tightness increases as well when

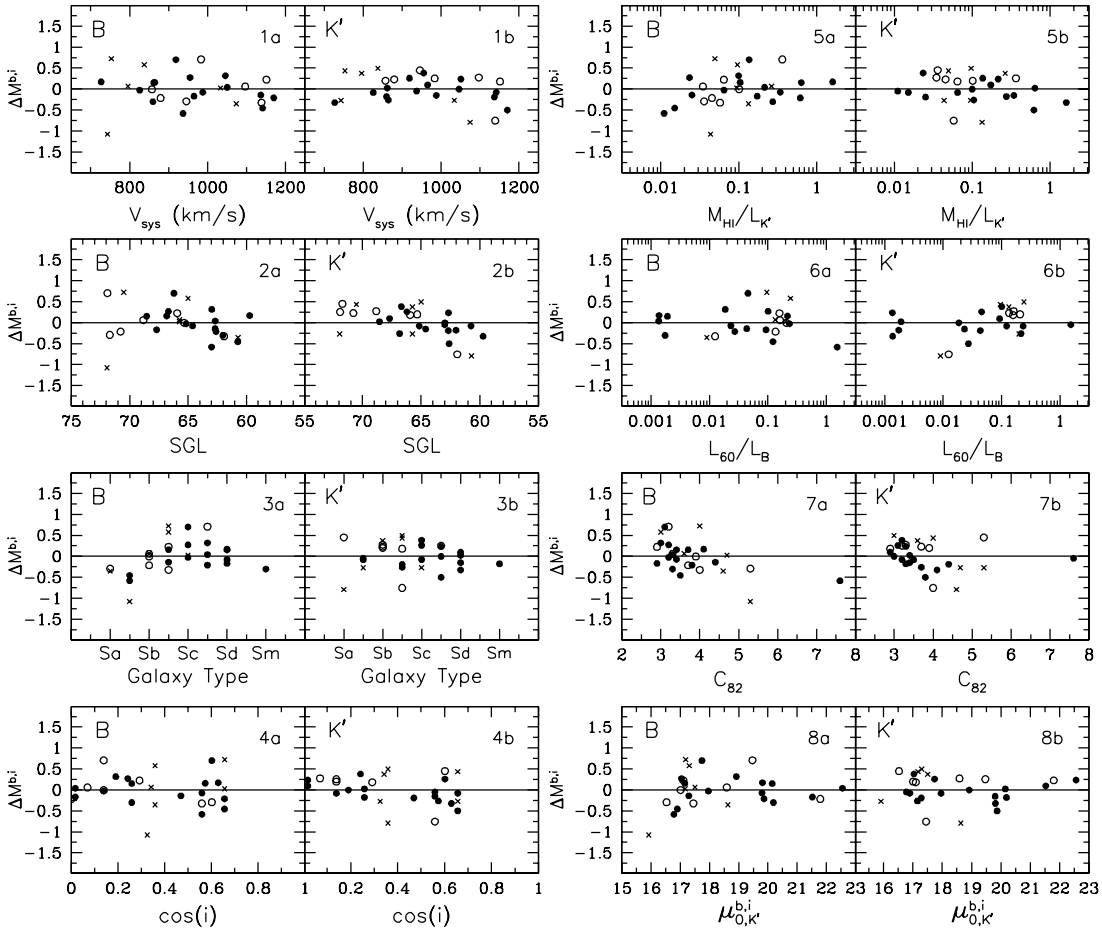

Figure 8: (**B**) Same as Figure 8a but now the residuals in the B,K'-V_{flat} TF-relations themselves are considered as a function of various global properties of the spiral galaxies in the *unperturbed sample*. Note that the filled circles remain on their positions but that the open symbols have moved upward and the open triangles are omitted because V_{flat} could not be measured in those galaxies.

using V_{flat} instead of V_{max} from the rotation curve. Unfortunately, a tighter relation in the near-infrared does not result in an improved distance estimater. A steeper slope in the near-infrared cancels the merits of a tighter correlation because the scatter is related to the slope. Consequently, the scatter is not reduced in the near-infrared.

For the sceptics among you, Figure 7 provides a blow-up of the I-band panel in the middle row of Figure 6. Each symbol is labeled with the NGC or UGC numbers used in the various tables throughout this book. This allows to relate each individual point to its observational material presented in Chapters 1 and 3. Note UGC 6969, for instance, the faintest object in Figur 7. One may argue that this point rules out the hypothesis that all galaxies with rising rotation curves would lie on the TF-relation if only their HI disks would have been extended enough to reach into the flat part of the rotation curve. The HI data of this galaxy show, however, that the last measured point very uncertain and consequently, the error bar on this point allows the galaxy to lie on the relation.

In Figures 8a and 8b we investigate whether the residuals in the M-V_{flat} TF-relations, as plotted in the lower panels of Figure 6, correlate with various global properties of the spirals. We consider only the *B*-band and *K′*-band residuals as extreme cases. In Figure 8a we calculated the deviations from the M-V_{flat} relations when using V_{max} and in Figure 8b we consider the residuals in the M-V_{flat} relations themselves. Consequently, the locations of the filled circles in Figure 8b are identical to those in Figure 8a while the open circles in Figure 8a have shifted upward in Figure 8b. Naturally, the open triangles in Figure 8b are absent. When looking for any trends in the residuals with other global properties, the open triangles and crosses should be

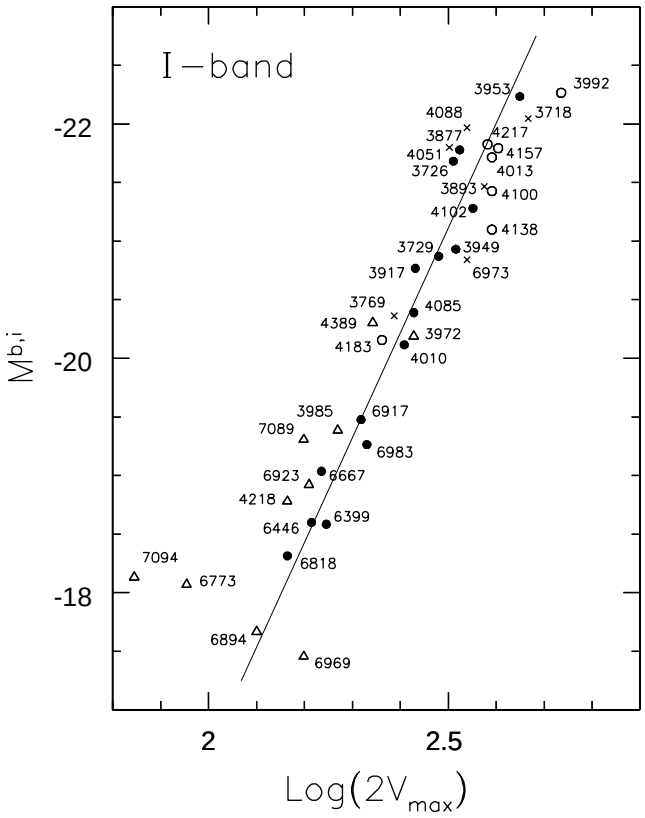

Figure 7: Enlargement of the I-band panel in the middle row of Figure 6. Here, the symbols are labeled with a galaxy's NGC or UGC number to allow checking with the photometric and HI synthesis data. NGC numbers run from 3718 through 4389, UGC numbers run from 6399 through 7094.

discarded because the deviations of the open triangles are not related to the underlying potential of a galaxy but merely to the extent of the HI disk. The crosses in both figures represent galaxies with perturbed kinematics. Because these galaxies are in a kinematically non-equilibrium situation their rotational velocities are also unlikely to relate to the underlying potential. Therefore, the crosses are best to be ignored as well when looking for trends in the panels of Figures 8a,b.

First, let us investigate whether the residuals correlate with the position of a galaxy in the cluster (panels 1a,b and 2a,b in both figures). Figure 1 hinted at a possible corelation between radial velocity and Super-Galactic longitude. In Figures 8a,b, no significant correlations are found in the *B*-band relations. In the K'-band, however, there seems to be a significant correlation of the V_{flat}-residuals with Super-Galactic longitude in the sense that galaxies at smaller Super-Galactic longitudes (northern part of the cluster) are too faint and galaxies at larger longitudes (southern part of the cluster) too bright (panel 8b-2b). This suggests that the northern part of the Ursa Major cluster is further away than the southern part. This is also something one would expect given the lower panel of Figure 1 and assuming that the spirals still feel the overall Hubble flow; galaxies in the northern part of the cluster tend to have higher recession velocities. Note, however, that a possible correlation of the residuals with recession velocity is insignificant (panel 8b-1b).

The strongest correlation that we find is with morphological type in the *B*-band (panels 8a,b-3a); early-type spirals are too faint in their blue light or rotate too fast compared to late type spirals. This effect is less visible when using V_{flat} instead of V_{max} but still present. Because this correlation is absent when using K' magnitudes, we interpret this effect as due to different stellar populations between early and late type spirals of the same luminosity and not due to differences in the maximum rotational velocity of dark matter haloes. If early type spirals would reside in more massive haloes, we would have anticipated the same effect in the K' residuals.

We find no correlations of the *B*-band and K'-band residuals with inclination.

A marginal correlation is found between the *B*-band residuals and the relative HI content of a spiral expressed in $M_{HI}/L_{K'}$ when considering V_{max} from the rotation curve (panel 8a-5a). Galaxies which are poorest in their relative HI content tend to be too faint in their blue light. However, this correlation can not be claimed when considering V_{flat} (panel 8b-5a). Note also that the apparent correlation in panel 8a-5a is mainly due to the HI poor early type spirals.

Panels 6a,b show that there is no correlation of the residuals with the 60μm flux from IRAS, normalized to the blue luminosity.

Considering only the open and filled circles in panels 7a,b, there might be a weak correlation between the residuals and the compactness of the light distribution, expressed in $C_{82}=R_{80}/R_{20}$ which is the ratio between the radii that enclose 80% or 20% of the total light. Galaxies with a substantial bulge or with a bright active nucleus have larger values of C_{82}. Panels 8a-7a,b indicate that compact systems tend to rotate faster than less compact systems. The most compact system with C_{82}=7.6 on the extreme right is the LINER galaxy N4102 with a very bright nucleus.

Finally, we checked for a possible correlation of the residuals with the face-on central surface brightness at K' of the exponential disk. We do not see any convincing trend.

6 Intrinsic scatter

The intrinsic scatter in the TF-relation is an elusive concept and its meaning depends on the context in

Table 8: 95% confidence intervals for the intrinsic scatter assuming that the depth of the cluster adds 0.17 mag in quadrature to the total observational uncertainties scatter. The three numbers for each entry refer to the minimum, the most likely and the maximum intrinsic scatter.

		95% confidence intervals for $\sigma_{\rm intr}$					
		equal weights			unequal weights		
		$W^i_{R,I}$	$2V_{max}$	$2V_{flat}$	$W^i_{R,I}$	$2V_{max}$	$2V_{flat}$
Westerbork Sample							
N=38	B	0.33 – 0.42 – 0.45	0.34 – 0.43 – 0.45		0.32 – 0.41 – 0.53	0.30 – 0.40 – 0.53	
	R	0.32 – 0.40 – 0.45	0.34 – 0.44 – 0.45		0.31 – 0.40 – 0.51	0.27 – 0.38 – 0.52	
	I	0.34 – 0.43 – 0.45	0.38 – 0.44 – 0.62		0.34 – 0.43 – 0.55	0.30 – 0.42 – 0.57	
	K′	0.40 – 0.44 – 0.64	0.44 – 0.60 – 0.76		0.40 – 0.50 – 0.64	0.38 – 0.52 – 0.70	
N=28	B	0.32 – 0.42 – 0.56	0.29 – 0.40 – 0.45	0.24 – 0.34 – 0.45	0.32 – 0.42 – 0.45	0.27 – 0.38 – 0.45	0.21 – 0.32 – 0.46
	R	0.24 – 0.34 – 0.44	0.19 – 0.29 – 0.42	0.13 – 0.24 – 0.37	0.24 – 0.34 – 0.44	0.16 – 0.27 – 0.40	0.06 – 0.21 – 0.35
	I	0.24 – 0.34 – 0.44	0.18 – 0.28 – 0.42	0.12 – 0.24 – 0.37	0.25 – 0.34 – 0.44	0.15 – 0.26 – 0.40	0.06 – 0.21 – 0.35
	K′	0.24 – 0.34 – 0.45	0.14 – 0.26 – 0.40	0.00 – 0.21 – 0.35	0.25 – 0.35 – 0.45	0.13 – 0.26 – 0.39	0.03 – 0.20 – 0.34
Healthy Sample							
N=32	B	0.28 – 0.37 – 0.45	0.30 – 0.40 – 0.45		0.27 – 0.36 – 0.48	0.26 – 0.36 – 0.45	
	R	0.30 – 0.39 – 0.45	0.33 – 0.43 – 0.45		0.28 – 0.38 – 0.45	0.25 – 0.37 – 0.45	
	I	0.33 – 0.43 – 0.45	0.38 – 0.44 – 0.65		0.33 – 0.42 – 0.56	0.30 – 0.43 – 0.45	
	K′	0.41 – 0.44 – 0.68	0.44 – 0.63 – 0.82		0.41 – 0.44 – 0.68	0.41 – 0.44 – 0.76	
N=22	B	0.24 – 0.35 – 0.45	0.22 – 0.33 – 0.48	0.13 – 0.25 – 0.39	0.24 – 0.35 – 0.45	0.21 – 0.32 – 0.47	0.09 – 0.23 – 0.37
	R	0.17 – 0.27 – 0.41	0.10 – 0.23 – 0.37	0.00 – 0.13 – 0.28	0.18 – 0.28 – 0.41	0.10 – 0.22 – 0.36	0.00 – 0.12 – 0.27
	I	0.18 – 0.29 – 0.42	0.08 – 0.22 – 0.37	0.00 – 0.14 – 0.30	0.19 – 0.29 – 0.43	0.10 – 0.22 – 0.37	0.00 – 0.14 – 0.29
	K′	0.20 – 0.32 – 0.44	0.00 – 0.21 – 0.37	0.00 – 0.11 – 0.30	0.22 – 0.33 – 0.45	0.11 – 0.24 – 0.38	0.00 – 0.16 – 0.31
Distance Sample							
N=15	B	0.10 – 0.21 – 0.37	0.00 – 0.15 – 0.32		0.06 – 0.20 – 0.36	0.00 – 0.13 – 0.31	
	R	0.07 – 0.20 – 0.36	0.00 – 0.07 – 0.27		0.07 – 0.20 – 0.36	0.00 – 0.00 – 0.26	
	I	0.11 – 0.24 – 0.40	0.00 – 0.10 – 0.30		0.12 – 0.24 – 0.41	0.00 – 0.09 – 0.30	
	K′	0.13 – 0.27 – 0.44	0.00 – 0.00 – 0.26		0.16 – 0.28 – 0.46	0.00 – 0.00 – 0.25	
N=13	B	0.11 – 0.24 – 0.42	0.00 – 0.17 – 0.36	0.00 – 0.13 – 0.32	0.09 – 0.23 – 0.41	0.00 – 0.16 – 0.35	0.00 – 0.10 – 0.31
	R	0.09 – 0.23 – 0.41	0.00 – 0.10 – 0.31	0.00 – 0.00 – 0.28	0.09 – 0.23 – 0.41	0.00 – 0.06 – 0.29	0.00 – 0.00 – 0.26
	I	0.13 – 0.26 – 0.44	0.00 – 0.14 – 0.35	0.00 – 0.07 – 0.32	0.14 – 0.27 – 0.46	0.00 – 0.12 – 0.34	0.00 – 0.07 – 0.32
	K′	0.15 – 0.30 – 0.45	0.00 – 0.00 – 0.32	0.00 – 0.00 – 0.25	0.18 – 0.31 – 0.53	0.00 – 0.01 – 0.31	0.00 – 0.00 – 0.26
Only galaxies with $V_{max} = V_{flat}$.							
N=15	B	0.20 – 0.32 – 0.52	0.11 – 0.25 – 0.44	0.11 – 0.25 – 0.44	0.20 – 0.33 – 0.52	0.04 – 0.23 – 0.43	0.04 – 0.23 – 0.43
	R	0.14 – 0.26 – 0.44	0.00 – 0.14 – 0.33	0.00 – 0.14 – 0.33	0.15 – 0.27 – 0.44	0.00 – 0.11 – 0.32	0.00 – 0.11 – 0.32
	I	0.15 – 0.28 – 0.44	0.00 – 0.14 – 0.34	0.00 – 0.14 – 0.34	0.17 – 0.29 – 0.44	0.00 – 0.11 – 0.32	0.00 – 0.11 – 0.32
	K′	0.12 – 0.27 – 0.44	0.00 – 0.00 – 0.20	0.00 – 0.00 – 0.20	0.16 – 0.29 – 0.44	0.00 – 0.00 – 0.18	0.00 – 0.00 – 0.18

which it is discussed. We have seen that the statistical properties of the TF-relation are closely related to the passband in which the luminosities are derived and to the selection criteria by which means a sample of galaxies is constructed. Therefore, extreme care should be taken if one tries to relate the intrinsic scatter to a certain degree of non-circular motions induced by non-spherical haloes when the intrinsic scatter is derived from a sample which is critically selected and optimized to serve as a distance tool (e.g. Franx and de Zeeuw, 1992). On the other hand it would be unfair to relate the intrisic scatter to the degree of accuracy with which distances can be measured if the intrinsic scatter is derived from a complete volume limited sample without any further selection criteria applied. We have seen, for instance, that the critically selected *normal spiral sample* yields a much tighter correlation than the *Westerbork sample*.

Here we calculated the 95% confidence intervals for the intrinsic scatter $\sigma_{\rm intr}$, given our estimated error budget. These intervals indicate the minimum and maximum values of $\sigma_{\rm intr}$ that can be accommodated within the total observed scatter. The results for the various passbands, samples, kinematic measures and fits are collected in Table 8. The minimum scatter, the most likely scatter and the maximum scatter is given for each entry. In some cases, the total observed scatter can be explained given the observational uncertainties: no additional intrinsic scatter would be required. Note that, in general, the confidence intervals become broader with smaller numbers of galaxies in a sample.

It should be noted again that the derived intrinsic scatters depend on the assumed depth of the cluster which is estimated to be $\sigma_{\rm depth}$=0.17 mag. In principle, however, $\sigma_{\rm depth}$ and the intrinsic scatter $\sigma_{\rm intr}$ can not be separated.

While reading the previous sections, it may have become clear that the scatter in the TF-relation can be dramatically decreased by applying proper selection criteria and especially when detailed knowledge about the kinematics of individual spirals is available. If only global profiles are available (W^i_R) and one insists on using every single galaxy (*Westerbork sample*, N=38) regardless of their morphology and shape of the global profile, one should prefer optical magnitudes and anticipate an intrinsic scatter of about 0.42$\pm$0.05 mag or a distance uncertainty of 19%. However, if one is willing to apply selection criteria, based on global properties (*normal spiral sample*, N=15), the intrinsic scatter can be reduced to 0.22$\pm$0.04 mag in the preferred optical bands. This corresponds to a relative distance uncertainty of 10%.

If one is patient enough and willing to embarque on a quest for detailed kinematic information of individual spirals, the usefulness of the TF-relations as a distance tool can be improved further. Measuring HI rotation curves from galactic velocity fields enables one to identify galaxies with rotation curves that are still rising at the last measured point and galaxies which show kinematic signs of interaction or global non-circular motions. Rejecting those galaxies will yield a sample of kinematically well behaved gas disks. Galaxies with a declining part in their rotation curve can be identified and for these systems the peak rotational velocity $V_{\rm max}$ can be discriminated from the amplitude of the flat in the outer region $V_{\rm flat}$. From Table 8 (*normal spiral sample*, N=22) we see that using $V_{\rm flat}$ instead of $V_{\rm max}$ results in significantly lower values for the intrinsic scatter. Moreover, the intrinsic scatter that can be accommodated in the K' relation is now comparable to the scatter on the *R* and *I* relations. The inferred intrinsic scatter in the *B*-band exceeds the ones in the other bands significantly. Using $V_{\rm flat}$ and *R*, *I* or K' magnitudes yields an intrinsic scatter of roughly 0.13 mag which corresponds to a relative distance uncertainty of 6%.

In practice, however, the distance uncertainty depends on the measured scatter. The smallest observed scatters are obtained in the *R* and *I* passbands and are typically 0.28 mag. These bands offer the best compromise between photometry accuracy, uncertain extinction corrections and the steepness of the slope. Subtracting $\sigma_{\rm depth}$ in quadrature yields a scatter of 0.22 mag or a relative distance uncertainty of 10%.

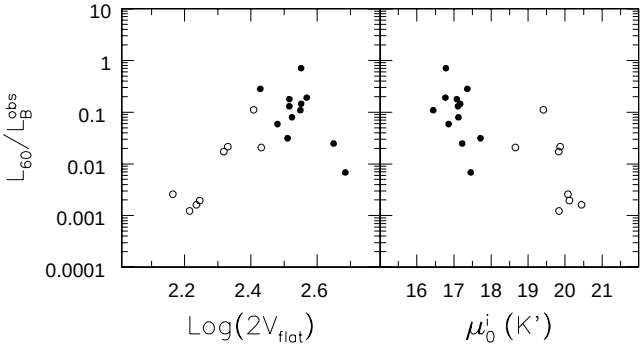

Figure 10: Relative dust content as a function of $V_{\rm flat}$ and central surface brightness in the K'-band. The less massive Low Surface Brightness galaxies (open symbols) have a relatively low dust content.

7 Low Surface Brightness galaxies and the TF-relation

It was shown by Zwaan *et al* (1995) that Low Surface Brightness (LSB) and High Surface Brightness (HSB) galaxies of the same luminosity lie on the same location in the TF-relation. Figure 9 shows the M–$V_{\rm flat}$ TF-relations for our sample and the solid lines indicate

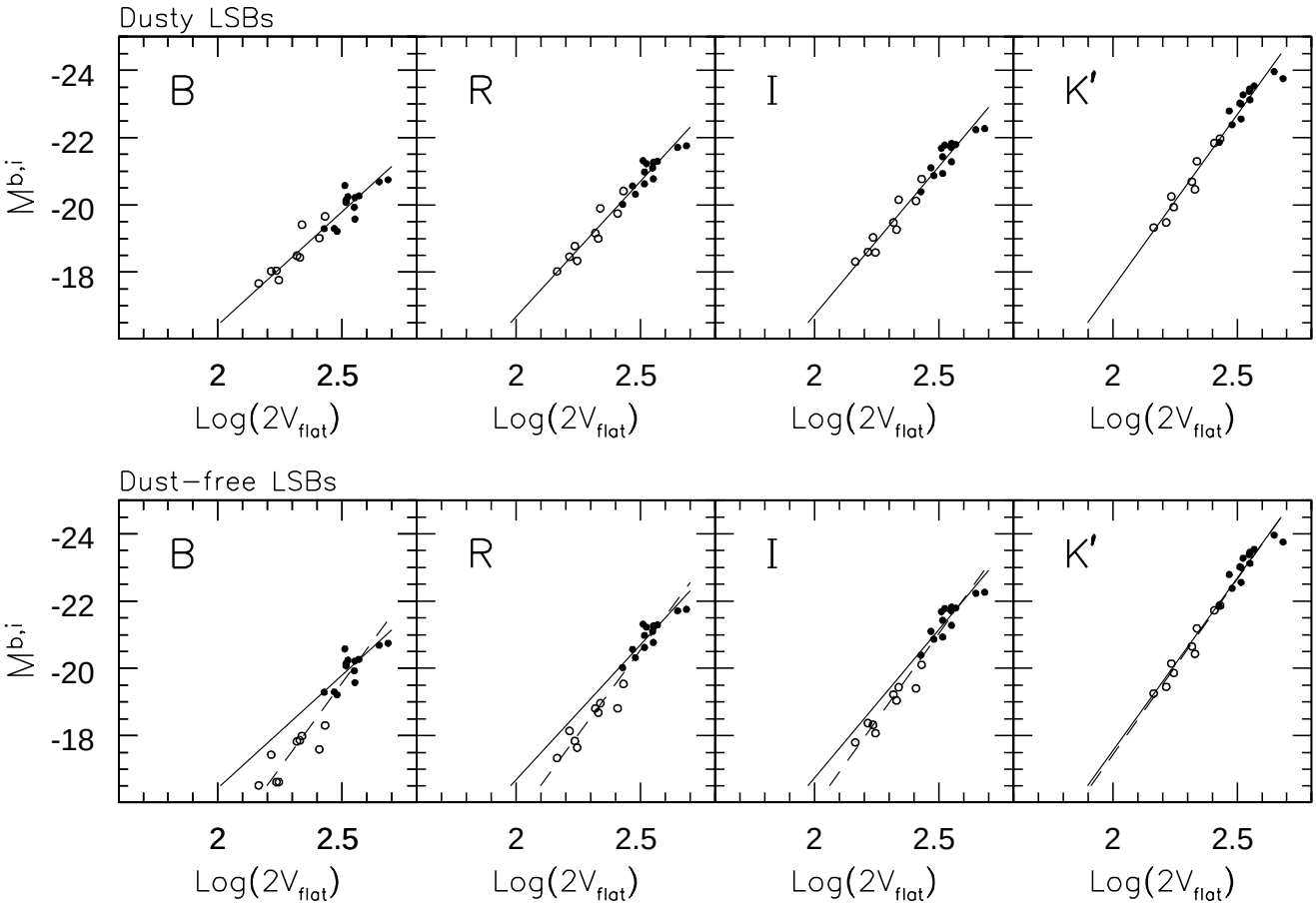

Figure 9: This figure illustrates how Low Surface Brightness galaxies (open circles) and High Surface Brightness galaxies (filled symbols) line up in the same TF-relation. In the upper panel, the same corrections for internal extinction are applied to both the LSB and HSB galaxies, in which case, there is no significant offset. In the lower panels, however, the LSB galaxies are assumed to be transparent at all wavelengths and no correction for internal extinction was applied. The filled symbols are located at the same position for each passband.

the fits. Here, the open symbols indicate the low surface brightness (LSB) galaxies as identified by Tully and Verheijen (1997) (Chapter 2, Paper II). In the upper panels, HSB and LSB galaxies received the same corrections for internal extinction. We confirm the result by Zwaan *et al* and extend it to the near-infrared. The slope in the K'-relation is very close to -10 and becomes as shallow as -6.7 in the B-band.

We note, however, that LSB galaxies contain in general much less dust than HSB galaxies. This is illustrated in Figure 10 where we plot the IRAS 60μm flux, normalized by the observed uncorrected blue luminosity, against log2V_{flat} and central surface brightness. There is a correlation between relative dust content, indicated by L_{60}/L_B and surface brightness. Therefore, in the spirit of Chapter 2, we assume that LSB galaxies are nearly transparent and construct the M–V_{flat} TF-relations without correcting the magnitudes of the LSBs for internal extinction. These TF-relations are plotted in the lower panels of Figure 9 in which the HSB galaxies still received an appropriate correction. Consequently, the filled symbols lie at the same location in the upper and lower panels but the open circles lie higher up in the upper panels. The solid lines in the lower panels are identical to the ones in the upper panels and the dashed lines indicate the new fits. The differences in slope and scatter are tabulated below.

	Dusty LSBs		Dust-free LSBs	
	slope	σ^{rms}	slope	σ^{rms}
B	-6.7±0.4	0.32	-10.1±0.4	0.47
R	-8.0±0.4	0.26	-10.1±0.4	0.35
I	-8.8±0.4	0.28	-10.3±0.4	0.33
K'	-10.3±0.4	0.29	-10.5±0.5	0.29

Note that under the assumption that LSB galaxies are dust-free, the slope of the relation is -10 in all passbands. Note, however, that such a bimodal extinction

correction is an extreme situation. It is likely that the extinction correction is a more gradual function of luminosity or surface brightness.

8 Discussion

Our study is the first one that considers a *complete volume limited* cluster sample of galaxies for which HI velocity fields are obtained as well as multi-band optical and near-infrared imaging photometry. As such, our dataset is unique but nevertheless, we would like to know how our results compare to a few of many other studies which relate the shape of the rotation curves to the statistical properties of the TF-relation. These studies come in four flavors, depending on how the rotation curves are measured, either via HI synthesis observations or by means of optical spectroscopy and either with long slit spectroscopy (or its radio-equivalent) along the major axis or through observations of the full galactic velocity field. Each methodology has its limitations in the extent of the interpretation of the data. In the light of its scientific merit, however, the availability of extended HI velocity fields is the most fruitful.

Broeils (1992) collected accurate HI rotation curves from the literature for a sample of 21 field galaxies with HI velocity fields. About half of these galaxies show a significantly declining part. Using *B*-band magnitudes, he found scatters of 0.70 mag when using global profile widths, 0.66 mag when using V_{max} and 0.55 mag when using $V_{flat}$with slopes of -7.3, -8.3 and -8.5 respectively. Unfortunately, it is not clear which fitting method he applied. Although he had much larger scatters than we do (he used a nearby field sample with significant distance uncertainties), he found the same trend in the scatter and slope of the relation. We find, however, nearly identical slopes when using W^i_R and V_{max} thanks to a more appropriate value for the turbulent motion parameter W_t. Broeils also made short WSRT observations (equivalent to optical long-slit spectroscopy) of a sample of 48 nearby field galaxies. In this sample he did not identify galaxies with rising, flat or declining rotation curves but he merely measured a 'representative' rotational velocity and subsequently found no improvement in the TF-relation when using this velocity instead of the global profile width; scatters of 0.77 versus 0.81 mag and slopes of -6.6 and -6.3 respectively. He concluded that a reduction of the scatter can only be achieved with more information about the inclination angle to be derived from full HI velocity fields.

Several years later, Rhee (1996) supplemented the two samples of Broeils who, in the meantime, had published 7 more rotation curves derived from full velocity fields. Rhee himself analysed short WSRT observations of 60 more spirals. With these larger samples of 28 velocity fields and 108 short observations, Rhee and Broeils (1996) reached exactly the same conclusions as Broeils did before: rotation curves derived from 'long-slit' HI observations are not helpful to reduce the scatter due to a lack of information about the inclination of a galaxy. This inclination angle and its possible change with radius can be retrieved from an HI velocity field, however, and that is why they advocate the use of full galactic velocity fields for deriving accurately the rotational velocity of a galaxy.

The investigations by Broeils and Rhee are the only ones so far that exploit the advantages of HI synthesis observations in an attempt to gain a better understanding of the statistical properties of the TF-relation. This is mainly because the reduction and interpretation of HI synthesis data is very elaborate. And indeed, studies using optical observations occur more frequently. The major advantage of optical spectroscopy is the much higher spatial resolution of the data compared to that of radio synthesis data. The disadvantages of optical spectroscopy, however, are the relatively low velocity resolution, the limited radial coverage and the influence of obscuring dust in the observed galaxies. Nevertheless, many investigators used Hα long-slit spectroscopy to retrieve the rotation curve of a galaxy (e.g. Rubin *et al* (1985), Courteau (1992), Mathewson *et al* (1992), Vogt *et al* (1996), Raychaudhury *et al* (1997) and many references therein).

Rubin *et al* (1985) noted a morphological segregation in the *B*- and *H*-band TF-relation obtained using V_{max} from their optical rotation curves. They constructed separate TF-relations for Sa, Sb and Sc type spirals selected from the nearby field and noted that, although the slopes are similar for each morphological class, in the *B*-band, earlier type spirals are offset toward higher rotational velocities with respect to later type spirals. This offset is less but not zero when using *H*-band magnitudes. Their rotation curves do not reach beyond R_{25} and a decline in the rotation curve beyond this radius, as is seen in the case of N3992 (see Figure 2), would not have been detected by them. They did not have the possibility to explore the shapes of the rotation curves in the outer regions. Furthermore, they found rather large scatters of 0.7 mag in both passbands after shifting the three separate relations on top of each other. These results of Rubin *et al* can be reconciled with our findings by noting that declining rotation curves are mainly found in early type spirals. It was impossible for Rubin *et al* to measure the rotation curve at large enough distances from the center to reveal a significantly declining part as we do. Apparently, in most cases, the relevant kinematic information is found in the very outer parts of the rotation curves, beyond R_{25}.

Recently, Raychaudhury *et al* (1997) investigated the *I*-band TF-relation for a sample of spirals in the

Coma cluster using long-slit Hα spectroscopy. They found, for a sample of 25 carefully selected Sb-Sd spirals, an unusually shallow slope of -5 and a remarkably low scatter of only 0.14 mag, barely consistent with their observational uncertainties. They investigated whether the scatter could be reduced even further by using the shape of the rotation curve as an extra parameter. They quantified the shape in terms of the steepness of the rotation curve in the *inner* part and, not surprisingly, failed to reduced the scatter any further. Due to a lack of signal, they were not able to measure the shape of the rotation curve in the outer regions.

Schommer *et al* (1993) present an extensive study using Fabry-Perot techniques to map the Hα velocity fields of 75 spirals in 3 clusters. By fitting tilted-rings to the velocity fields, they derive rotation curves from which they extract the circular velocity. A comparison of these circular velocities with the velocities derived from global HI profiles shows that the Hα velocities are often estimated too low. From their published rotation curves, we note that many are still rising at their last measured points and for those cases, it is likely that a more extended HI disk would show a significantly faster rotation in the outer regions. Unfortunately, they did not check whether the deviations between the optically and HI derived rotational velocities are related to the slope of the optical rotation curves at the last measured points. Anyway, using *I*-band magnitudes, they constructed TF-relations for 7 galaxies in the Antlia cluster and for 10 galaxies in the Hydra cluster. From double regression fits, they find scatters of 0.18 and 0.29 mag for the two clusters with slopes of -8.8$\pm$0.8 and -9.8$\pm$0.8 respectively.

Reviewing these studies of the TF-relation which make use of available rotation curves, illustrates that measuring rotation curves via optical spectroscopic gives insufficient information about the shape of rotation curves in the relevant outer regions of spirals.

The TF-relation is tighter in the near-infrared than it is at optical wavelengths. For distance measurements, however, the steeper slope in the near-infrared cancels the merit of the tighter relation in terms of the related scatter. Consequently, the near-infrared TF-relation does not provide a better distance tool compared to the TF-relation in the optical passbands.

On the other hand, the near-infrared luminosity is more closely related to the mass of the stellar population than the optical luminosities are. The observation that the correlation becomes increasingly tighter from the *B*-band to the K'-band suggests that the stellar mass itself is closely related to the gravitational potential. Moreover, using V_{flat} instead of V_{max} yields an even tighter correlation at K'. This indicates that the potential of the dark matter halo is closer related to the K'-band luminosity than the depth of the potential of the luminous mass itself.

The TF-relations seem to reflect a correlation between the potential of the dark matter halo and the stellar mass embedded in that halo, regardless of its distrubution.

9 Summary

This study has shown that the corrected widths of global HI profiles do provide the maximum rotational velocity observed in the HI rotation curves with a scatter of 6.8 km/s, provided that the proper correction for turbulent motion is applied. However, for galaxies with rotation curves that are still rising at the last measured point, neither the corrected line widths nor the *observed* maximum rotational velocity are good indicators of the actual maximum rotational velocity induced by the halo but merely yield lower limits. For galaxies with a partly declining rotation curve, the amplitude of the flat part in the outer regions can not be measured reliably from the width of the global profiles and depends on the surface density distribution of the HI gas.

For a complete volume limited sample, the total observed scatter in the TF-relation is typically 0.40 mag at the *B*, *R* and *I* passbands and 0.45 mag at K' when using the corrected widths of the global HI profile, after subtracting in quadrature the estimated contribution σ_{depth} due to the depth of the sample. From HI synthesis observations it is possible to evaluate the shapes of rotation curves and to identify galaxies with rising, flat or declining rotation curves. For galaxies with a declining rotation curve, a distinction can be made between V_{max} and V_{flat}. When using V_{max} as derived from the rotation curves, it is shown that galaxies with a constantly rising rotation curve lie systematically on the low velocity side of the TF-relation while galaxies with a declining rotation curve tend to lie on the high velocity side. Using V_{flat} instead of V_{max} for galaxies with declining rotation curves shows that they lie on the same TF-relation defined by galaxies for which $V_{max} = V_{flat}$. Excluding kinematically perturbed galaxies and considering V_{flat} instead of the corrected global line widths, the lowest scatter is found in the *R* and *I* passbands with an observed scatter of 0.28 mag.

The TF-relations steepen and becomes tighter going from *B*–band luminosities to the near-infrared. Using K' magnitudes and V_{flat}, the slope reaches -10 and the total observed scatter is consistent with no intrinsic scatter given the observational uncertainties.

High and Low Surface Brightness galaxies lie on the same TF-relation, also in the near-infrared. A morphological dependence of the zero point of the TF-relation can in part be understood when realizing that $V_{max} > V_{flat}$ in general occurs in compact, massive

early type spirals. The morphological dependence disappears at K' when using V_{flat} instead of V_{max}.

Acknowledgements

This research has been supported by NATO Collaborative Research Grant 940271, Grants from the US National Science Foundation and the Leids Kerkhoven-Bosscha Fonds. The Westerbork Synthesis Radio Telescope is operated by the Netherlands Foundation for Research in Astronomy (NFRA) with financial support from the Netherlands Organization for Scientific Research (NWO).

References

Beers, T.C., Flynn, K. and Gebhardt, K., 1990, A.J. 100, 32

Begeman, K., 1989, A.&A., 223, 47

Bernstein, G.M., Guhathakurta, P., Raychaudhury, S., Giovanelli, R., Haynes, M.P., Herter, T. and Vogt, N.P., 1994, A.J. 107, 1962

Bernstein, G.M., Guhathakurta, P., & Raychaudhury, 1996, in *"Spiral Galaxies in the Near-IR"*, Minniti, D. & Rix, H.-W. (eds.), Springer-Verlag, Berlin

Bottinelli, L., Gouguenheim, L., Paturel, G. and de Vaucouleurs, G., 1983, A.&A., 118, 4

Bottinelli, L., Gouguenheim, L., Fouqué, P. and Paturel, G., 1990, A.&A.Suppl., 82, 391

Bottinelli, L., Gouguenheim, L., Paturel, G., Renaud, N. and Witasse, O., A.&A., in preparation

Broeils, A.H., 1992, Thesis, University of Groningen

Casertano, S., & van Gorkom, J.H., 1991, AJ, 101, 1231

Courteau, S., 1992, PhD thesis, University of California at Santa Cruz

Fisher, J.R. and Tully, R.B., 1981, Ap.J.Suppl., 47, 139

Fouqué, P., Bottinelli, L., Gouguenheim, L. and Paturel, G., 1990, Ap.J., 349, 1

Franx, M. and de Zeeuw, P.T., 1992, Ap.J., 392, L47

Holmberg, E., 1946, Medd. Lunds Astr. Obs., Ser.II, No.117

Hubble, E., 1926, Ap.J., 64, 321

Mathewson, D.S., Ford, V.L. and Buchhorn, M., 1992, ApJSuppl., 81, 413

Peletier, R.F., & Willner, S.P., 1993, ApJ, 418, 626

Pierce, M.J. and Tully, R.B., 1988, ApJ, 330, 579

Raychaudhury, S., von Braun, K., Bernstein, G.M. and Guhathakurta, P., 1997, A.J., 106, 113

Rhee, M.-H., 1996, Thesis, University of Groningen

Rieke, G.H. and Lebofsky, M.J., 1985, ApJ, 288, 618

Rubin, V.C., Burstein, D., Ford Jr, W.K. and Thonnard, N., 1985, Ap.J., 289, 81

Schommer, R.A., Bothun, G.D., Williams, T.B. and Mould, J.R., 1993, A.J., 105, 97

Tully, R.B. and Fisher, J.R., 1977, A&A, 54, 661

Tully, R.B. and Fouqué, P., 1985, Ap.J.Suppl., 58, 67

Tully, R.B., Verheijen, M.A.W., Pierce, M.J., Huang, J.-S., & Wainscoat, R.J., 1996, AJ, 112, 2471 (Paper I)

Tully, R.B. and Verheijen, M.A.W., 1997, ApJ, 484, 145 (Paper II)

van Albada, T.S., and Sancisi, R., 1986, Phil. Trans. R. Soc. Lond. A, 320,447

Vogt, N.P. Forbes, D.A., Phillips, A.C., Cronwall, C., Faber, S.M., Illingworth, G.D. and Koo, D.C., 1996, Ap.J., 465, L15

Zwaan, M.A., van der Hulst, J.M., de Blok, W.J.G., and McGaugh, S.S., 1995, MNRAS, 273, L35